Since January 2020 Elsevier has created a COVID-19 resource centre with free information in English and Mandarin on the novel coronavirus COVID-19. The COVID-19 resource centre is hosted on Elsevier Connect, the company's public news and information website.

Elsevier hereby grants permission to make all its COVID-19-related research that is available on the COVID-19 resource centre - including this research content - immediately available in PubMed Central and other publicly funded repositories, such as the WHO COVID database with rights for unrestricted research re-use and analyses in any form or by any means with acknowledgement of the original source. These permissions are granted for free by Elsevier for as long as the COVID-19 resource centre remains active.

Journal of Molecular Structure 1264 (2022) 133190

Contents lists available at ScienceDirect

Journal of Molecular Structure

journal homepage: www.elsevier.com/locate/molstr

An unexpected single crystal structure of nickel(II) complex: Spectral, DFT, NLO, magnetic and molecular docking studies

Wassila Derafa[a,b], Djouhra Aggoun[a,c,*], Zakia Messasma[a,c], Selma Houchi[d,e], Sofiane Bouacida[f,g], Ali Ourari[a]

[a] Laboratory of Electrochemistry, Molecular Engineering and Redox Catalysis, Department of Process Engineering, Faculty of technology, University of Ferhat Abbas, Setif 19000, Algeria
[b] Chemistry Department, College of Science, Jouf University, Sakaka 72388, Saudi Arabia
[c] Chemistry Department, Faculty of sciences, University Ferhat Abbas, Setif 19000 Algeria
[d] Laboratory of Applied Biochemistry, Faculty of Natural and Life Sciences, University Ferhat Abbas, Setif 19000 Algeria
[e] Department of Biochemistry Faculty of Natural and Life Sciences, University Ferhat Abbas, Setif 19000 Algeria
[f] Department of Sciences of Matter, Faculty of Exact Sciences, Oum El Bouaghi University, 04000, Algeria
[g] Research Unit of Environmental Chemistry and Molecular Structural CHEMS, University of the Mentouri Brothers, Constantine, Algeria

ARTICLE INFO

Article history:
Received 5 March 2022
Revised 23 April 2022
Accepted 28 April 2022
Available online 30 April 2022

Keywords:
Dehydroacetic acid
Nickel complex
Magnetic susceptibility
DFT
Nonlinear optical properties
Molecular docking

ABSTRACT

This work explores the study of a synthesized nickel complex as a possible inhibitor against the main protease (Mpro) of the recent emerging coronavirus disease (COVID-19). Overall, the template reaction of 3-acetyl-2-hydroxy-6-methyl-4*H*-pyran-4-one with nickel(II) chloride hexahydrate in *N*,*N*-dimethylformamide (DMF) medium leads to the formation of neutral nickel complex. This resulting complex is formulated as $[Ni(DHA)_2(DMF)_2]$ on the basis of FT-IR, UV-Vis., single-crystal X-ray diffraction analysis, magnetic susceptibility and CV measurements as well as DFT quantum chemical calculations. Its single crystal suggests was found to be surrounded by the both pairs of molecules of DHA and DMF through six oxygen atoms with octahedral coordination sphere. The obtained magnetic susceptibilities are positive and agree with its paramagnetic state. In addition to the experimental investigations, optimized geometry, spectroscopic and electronic properties were also performed using DFT calculation with B3LYP/6-31G(d,p) level of theory. The nonlinear optical (NLO) properties of this complex are again examined. Some suitable quantum descriptors (E_{HOMO}, E_{LUMO}, Energy gap, Global hardness), Milliken atomic charge, Electrophilic potion and Molecular Electrostatic Potential) have been elegantly described. Molecular docking results demonstrated that the docked nickel complex displayed remarkable binding energy with Mpro. Besides, important molecular properties and ADME pharmacokinetic profiles of possible Mpro inhibitors were assessed by in silico prediction.

© 2022 Elsevier B.V. All rights reserved.

1. Introduction

Wuhan city, Hubei province of China, December 2019, a novel infectious Coronavirus disease (formally called COVID-19) caused by SARS-CoV-2 has been reported and raised as a global health anxiety. Two months later on March 11, 2020, World Health Organization (WHO) declared it as a pandemic after its hurried propagation in Chinese territory and also spread through the world [1]. Coronavirus, positive and single-stranded RNA, is one of the most viruses that can infect both humans and animals [2]. Until now, the most identified promising targets are the spike protein, RNA-dependent RNA polymerase (RdRp), and the 3-chymotrypsin-like protease (3CLpro) otherwise known as main protease (Mpro) [3,4]. It cleaves the polypeptide in to various non-structural proteins which are involved in the viral replication. Hence, it is essential for processing the polyprotein that led to the proteolytic activation of the viral functional proteins [5]. Consequently, now, the main promising target for researcher community is to obtain novel treatment of coronavirus disease based on synthetic compounds.

In coordination chemistry, dehydroacetic acid or 3-acetyl-2-hydroxy-6-methyl-4*H*-pyran-4-one (Abbreviated as DHA) and its derivatives are excellent reactive heterocyclic compounds [6]. Against a lot of organic compounds, DHA can serve as an important pharmacologically active intermediate in organic synthesis because of its several reactive functional groups compared to electrophilic and nucleophilic reagents [7]. Furthermore, this property makes of them a very promising advantage for researchers due

* Corresponding author at: Laboratory of Electrochemistry, Molecular Engineering and Redox Catalysis, Department of Process Engineering, Faculty of technology, University of Ferhat Abbas, Setif 19000, Algeria.
E-mail address: djouhra.aggoun@univ-setif.dz (D. Aggoun).

https://doi.org/10.1016/j.molstruc.2022.133190
0022-2860/© 2022 Elsevier B.V. All rights reserved.

to their wide-ranging biological properties such as fungicidal [8], bactericidal [9], antibiotic [10] and as well for a lot of their use in food technology preservative [11]. Additionally, major advances were made recently in the development of anti-viral therapy of DHA derivatives. As example, these compounds act efficiently in inhibiting diverse targets and as potential HIV protease inhibitors due to the interaction of dehydroacetic acid derivatives against HIV-1 integrase [12]. Other numerous properties and applications have also been known for DHA with its derivatives. These compounds are harmless as cosmetic ingredients in the current practice [13] and they are commonly known for their use in the enhancement and stabilization of vitamin C [14].

Therefore, metal complexes based on DHA that have exceptional chelating properties were synthesized and fully discussed in the literature [15]. Remarkably, it is acknowledged that the nickel complexes with Ni^{2+} are more active than either dehydroacetic acid ligand alone or the pure inorganic nickel salts [16]. As example, nickel(II) complexes of symmetrical and unsymmetrical Schiff bases containing dehydroacetic acid have been prepared and characterized by Tan and Ang [17]. Recently, the synthesis of α,β-unsaturated compounds derived from DHA and indol-3-carboxaldehyde has been particularly focused [18,19]. Also, F.A. El-Saied *et al.* have synthesized nickel(II) complexes, derived from DHA, N4-dialkyl and 3-azacyclothiosemicarbazones [20].

In the context of this current study and as a continuation of our previous works [21], we report herein the synthesis and determination of the crystal structure of the nickel(II) complex $[Ni(DHA)_2(DMF)_2]$ as mononuclear complex. The structural and spectral data of the prepared complex are presented with its magnetic properties which are also well discussed. As for the red/ox behavior of this nickel complex, it was investigated by cyclic voltammetry. Furthermore, this study is supported by some appropriate quantum parameters quantified by using the density functional theory (DFT). Hirschfeld surface analysis and HOMO/LUMO energy were also used to forecast the structural and spectroscopic parameters of this synthesized compound. Finally, the ADMET/tox studies and the binding affinity, of the $[Ni(DHA)_2(DMF)_2]$ complex with the key target main protease (M_{pro}) of SARS-CoV-2 through molecular docking analysis.

2. Experimental section

2.1. Materials and methods

In this study, the chemicals and solvents were used as received without any additional purification and were bought from Aldrich and Fluka. FT-IR spectra were recorded on Perkin and Elmer 1000-FT-IR Spectrometer using KBr disks, while the electronic spectra (UV-Vis.) were obtained on a Unicam UV-300 Spectrophotometer having 1 cm as a path length cell. Electrochemical experiments were performed on a voltalab 40, Potentiostat galvanostat controlled by microcomputer. Thus, the cyclic voltammograms were recorded using an individual cell of 5 ml using a conventional three-electrode system in distilled H_2O + NaCl (10^{-1} M) and NaOH ($2{\cdot}10^{-1}$M) under nitrogen atmosphere. The working electrode was a disc of glassy carbon (diam. 3 mm) while the counter electrode was a platinum wire, and all potentials were expressed versus the saturated solutions of calomel electrode (SCE).

2.2. Chemistry

2.2.1. Synthesis

The synthesis of nickel complex was carried out in the same experimental conditions, early applied for copper complexes, as described in the literature [21,22]. The complex was obtained by mixing stoichiometric amounts of dehydroacetic acid 0.168 g (1mmol) with nickel(II) chloride hexahydrate ($NiCl_2{\cdot}6H_2O$) 0.238 g (1 mmol). To this mixture, 0.06 g (1 mmol) of ethylenediamine, dissolved in 10 ml of methanol, were slowly added. Then, an excess of pyridine 0.158 g (2 mmol) was dissolved in 5 ml of methanol. After two hours of reaction, a sky-blue precipitate was observed and recovered by filtration. It was then purified by successive washings using cold methanol and diethyl ether followed by drying over $CaCl_2$ to give a sky-blue powder. This blue powder was dissolved in hot *N,N*-dimethylformamide in which the suitable monocrystals of $[Ni(DHA)_2(DMF)_2]$ were formed by slow evaporation in 10 days.

Table 1
Crystal data, data collection and structure refinement parameters for of $[Ni(DHA)_2(DMF)_2]$ complex.

Compound	$[Ni(DHA)_2(DMF)_2]$
Empirical formula	$C_{22}H_{28}N_2NiO_{10}$
Formula weight	539.17
T (K)	150
λ (Å)	0.71073
Crystal system	Triclinic
Space group	P-1
a(Å), b(Å), c(Å)	7.7441 (10), 118.2173 (10), 119.5338 (12)
(°)α, (°)β, (°)γ	85.152 (7), 1185.953 (9), 1178.157 (9)
V (Å^3), Z	590.77 (13), 111
ρ (g cm^{-3})	1.516
μ (mm^{-1})	0.88
F(000)	282
Limiting indices	h = 11−99, k = 11−99, l = 11−1111
Data/restraints/ Parameters	4966/0/165
Goodness of fit on F^2	1.053
Final R index [$I > 2\sigma(I)$]	0.0555
R index [all data]	0.1665
Largest difference peak and hole (e Å^{-3})	0.735−0.724
CCDC deposition no.	2142076

$R = \{\Sigma[w(|F_o| - |F_c|)]/\Sigma w(|F_o|)\}$, $Rw = \{\Sigma w(|F_o| - |F_c|)^2]/\Sigma w(|F_o|^2)^{1/2}$
$wR2 = \{\Sigma[w(F^2{}_o - F^2{}_c)^2]/\Sigma w(F^2{}_o)^{1/2}$
$w = 1/\sigma^2(F_0{}^2) + (0.0794P)^2 + 0.6853P]$ where $P = (F_o{}^2 + 2F_c{}^2)/3$

2.2.2. Crystallography

The blue prism crystals of the nickel complex were obtained after redissolution of the resulting sky-blue powder followed by slow evaporation in hot *N,N*-dimethylformamide. X-ray data were collected with a Bruker Apex II CCD area detector, equipped with diffractometer using a graphite monochromated Mo-Kα radiation source (λ = *0.71073* Å) at 150 K. The crystallographic data and experimental details for structural analysis are summarized in Table 1. The described structure was resolved through direct methods with SIR2004 [23] to locate all the non-H atoms, which were anisotropically refined with SHELXL97 [24] and using full-matrix least squares on squared procedure from within the WINGX suite of software [25] used to prepare material for publication. All the H atoms were placed in the calculated positions and constrained to ride on their parent atoms. Drawings of molecules were produced with the program ORTEP-3 and Diamond [26,27].

2.3. Computational details

Computational study of $[Ni(DHA)_2(DMF)_2]$ complex were performed by Gaussian 09 along with Gauss View 5.0.8 for visualizations by using DFT method at the level of B3LYP/6-31G (d, p) basis set [28]. This basis set was one of the most acknowledged basis sets used in the study of medium and large sized hydrogen bonded systems, and also for yielding a very small Basis Set Superposition Error (BSSE) [29]. The geometries of this complex were fully optimized without any constraint on every bond length, bond angle and dihedral angle were compared with the crystalline structure. The optimized structures were confirmed to be local minima

by performing harmonic vibration frequency analyzes. Further analyzes of electronic and optical properties were carried out by calculation of UV-Vis. absorption in the framework of Time-Dependent DFT (TD-DFT) [30,31]. Under the same basic set, the highest occupied molecular orbital (HOMO) and the lowest unoccupied molecular orbital (LUMO) were as well achieved. The reactivity descriptors that include energy gap (ΔEgap), hardness (η), softness (S), global electronegativity (χ), electrophilicity (ω), molecular electrostatic potential (MEP), Mulliken atomic charge and NLO have also been computed.

2.4. Molecular docking

2.4.1. Molecular modelling platform

Molecular docking and ADME/Tox studies were performed using Molecular Operating Environment (MOE) version 2019.10 molecular modelling software and Discovery Studio (DS) 2.0 Software (Studio 2.5, Accelrys, Co. Ltd., San Diego, CA, USA), respectively.

2.4.2. Molecular docking studies

The protein data bank of the Research Collaboration for Structural Bioinformatics (RCSB), website (http://www.rcsb.org/pdb) was used to obtain the crystal structure the Main Protease (M_{pro}), also called 3C-like protease (3CLpro), which represents a pivotal role in the propagation of SARS-CoV–2. The crystal structure of this enzyme was downloaded in complex with its inhibitor N3, (PDB ID: 6LU7; 2.16 Å) [3].

2.4.3. Sample and protein structures preparation

Retrieval and protein structure preparation of active sites: The targets protein, Mpro (6LU7), used in this study, were protonated where hydrogen atoms were added with its 3D geometry, corrected for any found errors in the connection or type of different atoms, and then energy minimized at the end of the preparation steps. This step followed by site-finder to define and isolate the same binding pocket of the co-crystallized native inhibitor as dummy atoms over helix for the docking step.

Sample preparation: The 2D structure of the $[Ni(DHA)_2(DMF)_2]$ complex was drawn using Marvin software [32], converted to 3D and optimized by HyperChem 8.03 software [33]. Then, the energy minimizing of this compound was done under the following experimental conditions like temperature = 300 K and pH = 7. Furthermore, the geometry was performed using the field strengths in the MMFF94x implanted in MOE and Austin model 1 (AM 1) with gradient value of 0.0001 kcal/mol. Then, the compound was saved in mdb format as a new database.

2.4.4. Docking

After that the protein structures and ligands were minimized and the active binding site was located, the ligands were docked to the protein using the dock tool of Molecular Operating Environment (MOE) 2019.0102 software for fitting of the isolated $[Ni(DHA)_2(DMF)_2]$ complex database into the active site of SARS-CoV-2 Mpro enzyme. Docking site was selected as dummy atoms, alpha triangle as the placement methodology, and London dG as scoring methodology. The docking process was run followed by evaluation of poses. Poses with the highest energy scores and best ligand-enzyme interactions were selected and recorded.

2.5. Chemical descriptors calculation

Filters us Molecular weight of the ligand (<500 Da), high lipophilicity (Log *P*<5), number of hydrogen bonds donors (<5), number of hydrogen bond acceptors (<10) and lip druglike were used to investigate the monocrystal's drug-likeliness using the Lipinski's Rule of Five [34]. Parameter details were calculated using Molecular Operating Environment (MOE) 2019.0102 software.

2.5.1. ADME analysis

The $[Ni(DHA)_2(DMF)_2]$ complex were screened using Discovery Studio (DS) 2.0 Software (Studio 2.5, Accelrys, Co. Ltd., San Diego, CA, USA) to predict their important pharmacokinetic properties. The prediction of pharmacokinetics ADME (Absorption, Distribution, Metabolism, Excretion and Hepatotoxicity) properties include eight mathematical models, such as solubility and its level, HIA (human intestinal absorption), ADME AlogP98, ADME PSA-2D, BBB penetration level PPB (plasma protein binding), ADME CYP2D6 and hepatotoxicity.

2.5.2. Toxicity risks assessment

To determine the therapeutic compatibility of the drug, another method was used, toxicity prediction, by using the USFDA (US FDA, United States Food and Drug Administration) standard toxicity risk predictor software TOPKAT in the Discovery Studio. In this module, Ames mutagenicity, TOPKAT mouse female NTP, TOPKAT mouse male NTP probability and Daphnia EC_{50} were predicted via Discovery Studio (DS) 2.0 Software (Studio 2.5, Accelrys, Co. Ltd., San Diego, CA, USA).

3. Result and discussions

The complex was found air stable and insoluble in most of the common organic solvents but soluble in hot DMF and DMSO. The given formulation of this complex is based on crystal structure, infrared and UV-visible spectra, magnetic measurements, electrochemical analysis and theoretical studies. The structure of the synthesized complex is represented in the following Scheme 1.

3.1. Description of crystal structure

The good quality crystals of this nickel complex was crystallized by dissolving $[Ni(DHA)_2(DMF)_2]$ complex powder in *N,N*-dimethylformamide (DMF) under hot conditions until boiling point T = 140°C. The crystallization time was 15 days at room temperature. This nickel complex crystallizes in a triclinic space group P-1 system with a = 7.7441 (10) Å, b = 8.2173 (10) Å, 9.5338 (12) Å, α = 85.152 (7) °, β = 85.953 (9) °, γ = 78.157 (9) ° of volume V = 590.77 (13) $Å^3$ and Z = 1. An ORTEP view of the complex with the selective atom numbering scheme is shown in Fig. 1. A summary of the details about crystal data, collection parameters and refinement are documented in Table 1. The structure of the nickel complex reveals that it crystallizes with two molecules of the crystallization solvent (DMF). As shown in Fig. 1, each nickel(II) ion centre is six coordinated in a form of a distorted square-bipyramid environment. This octahedral coordination sphere is formed by the both deprotonated dehydroacetic acid ligands through their two ketone oxygen atoms and two phenoxy oxygen atoms and also coordinated by two DMF ligands. The bond distances and angles are summarized in Table 2.

The bond lengths involving the phenoxy oxygen (C4–O1), the phenyl carbon (C2–O2) and ketone carbon of DMF molecule (C9–O5) are 1.276 (4), 1.248 (4) and 1.325 (4) Å, respectively. These values were found to be in the range of those usually observed as standard of C(sp^2)–OH and C(sp^2)–O– bond length [35,36]. The six Ni–O bond lengths are 1.974 (2) and 2.003 (2) Å for DHA molecules and 2.108 (2) Å (Table 2). These values are in good agreement with related reported complexes [37,38]. The selected cis angles of the nickel environments deviate from their ideal values only for 90° angles and found to be in the ranges 87.65 (8)°–92.35 (9)° while, for trans angles, they were obtained with ideal values and equal to 180°.

The crystal packing for $[Ni(DHA)_2(DMF)_2]$ complex, can be described as an alternating layers parallel to (011) plane (See Fig. 2)

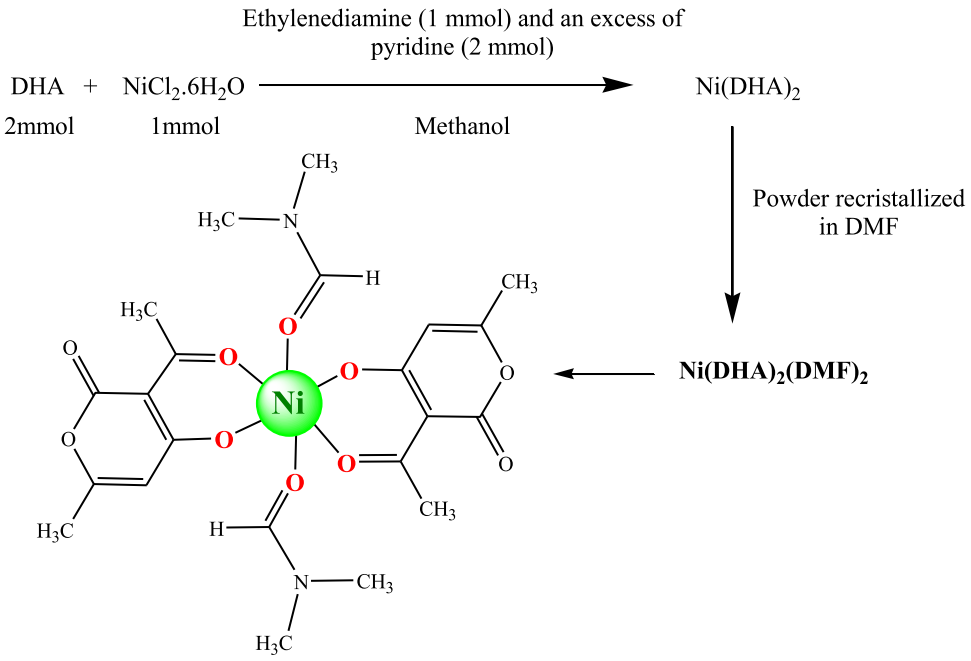

Scheme 1. Synthetic pathway for preparation of the Ni(II) complex with 3-acetyl-2-hydroxy-6-methyl-4*H*-pyran-4-one.

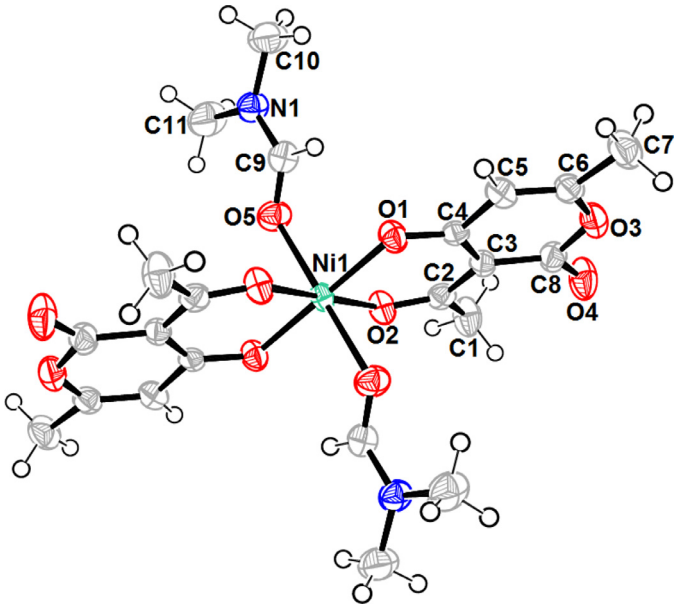

Fig. 1. The molecular geometry of $[Ni(DHA)_2(DMF)_2]$ complex. No labeled atoms are generated by inversion center symmetry (−x, −y, −z). Displacement ellipsoids are drawn at the 50% probability level. H atoms are represented as small spheres of arbitrary radius.

and molecules are also linked via C-H…O intermolecular hydrogen bonds forming an infinite three-dimensional network.

3.2. Computational procedures

3.2.1. Molecular geometry

Geometrical parameters of $[Ni(DHA)_2(DMF)_2]$ complex were determined with SC-XRD and B3LYP/6-31G(d,p) and collected in Table 2. The DFT optimized and X-ray structure of $[Ni(DHA)_2(DMF)_2]$ complex is shown in Fig. S1. The global minimum energy obtained by DFT structure optimization based on B3LYP/6-31G(d,p) basis set for $[Ni(DHA)_2(DMF)_2]$ complex as -3223.4385390 Hartrees. The optimized molecular structure of $[Ni(DHA)_2(DMF)_2]$ complex with the labelling of atoms is presented in Fig. 3. As it can be clearly seen from the Table 3, the experimental lengths involved in the phenoxy oxygen (C4–O1), the phenyl carbon (C2–O2) and ketone carbon of DMF molecule (C9–O5) are 1.276 (4), 1.248 (4) and 1.325 (4) Å, respectively. Whereas, the calculated values are 1.2807, 1.4764 and 1.215 Å, respectively. The Ni1-O1i, Ni1-O1, Ni1-O2, Ni1-O2i and Ni1-O5i experimentally determined bond lengths are equal to 1.974 (2), 1.974 (2), 2.003 (2), 2.003 (2), and 2.108 (2) Å, respectively. These values are closely equal to those corresponding to DFT calculated bonds ranging from 1.7931 to 1.9094 Å. In this work, computations have been done in the gas phase and experimental measurement has been carried out in the solid phase. Hence, the assessment of these outcomes confirmed that most of the simulated values are barely larger than the experimental values. In present work, most of the computed bond angles are absolutely larger than the experimental values due to the low scattering factor of hydrogen atoms participating in the X-ray diffraction experiment producing a huge deviation from the theoretical C−H bond lengths [39]. In this case, it can concluded that there is an acceptable agreement between the DFT calculated geometries and corresponding SC-XRD values by comparing, the structure of crystal of $[Ni(DHA)_2(DMF)_2]$ complex.

3.2.2. Vibrational assignments

The solid-state infrared spectrum has been recorded in the region of 4000-400 cm^{-1}. The corresponding theoretical spectrum has been calculated by using B3LYP level and 6-31G(d,p) basis set. The experimental and calculated vibrational spectra are given in Fig. 4. The experimental and theoretical vibrational wave numbers, FT-IR intensity and assignments of vibration modes have also been presented in Table 3. As shown in Fig. 4, the formation of this nickel complex has been confirmed by detecting the characteristic absorption band of lactone O–C=O group, observed at 1710 cm^{-1} [40]. The dehydroacetic acid containing as well C=O group would be presented as strong and sharp absorption band at 1690 cm^{-1} [41] while, those calculated were found at 1702 and 1734 cm^{-1}, respectively. In addition, the absorption band observed at 1352 cm^{-1}

Table 2
The experimental and calculated values of the bond lengths and bond angles of $[Ni(DHA)_2(DMF)_2]$ complex.

$[Ni(DHA)_2(DMF)_2]$ complex								
Bond lengths (Å)	X-ray	B3LYP	Bond lengths(Å)	X-ray	B3LYP			
C4–O1	1.276 (4)		Ni1-O2i	2.003 (2)	1.9094			
C2–O2	1.248 (4)		Ni1-O5i	2.108 (2)	1.8029			
C9–O5	1.325 (4)		Ni1-O1	1.974 (2)	1.81			
Ni1-O1i	1.974 (2)	1.8408	Ni1-O5	2.108 (2)	1.8429			
Ni1-O2	2.003 (2)	1.7931						
Bond angles (°)	X-ray	B3LYP	Bond angles (°)	X-ray	B3LYP	Bond angles (°)	X-ray	B3LYP
O2-Ni1-O5	91.31 (9)	102.52	O1i-Ni1-O1	180	176.326	O1i-Ni1-O5i	91.83(9)	105.151
O2i-Ni1-O5	88.69 (9)	76.25	O1i-Ni1-O2	92.35(9)	102.151	O1-Ni1-O5i	88.17 (9)	82.0802
O5i-Ni1-O5	180.0(13)	177.353	O1-Ni1-O2	87.65 (8)	102.115	O2-Ni1-O5i	88.69 (9)	86.1558
C4-O1-Ni1	127.7 (2)	125.5693	O1i-Ni1-O2i	87.65 (8)	101.872	O2i-Ni1-O5i	91.31 (9)	91.2787
C2-O2-Ni1	130.5 (2)	125.3	O1-Ni1-O2i	92.35 (9)	105.715	O1i-Ni1-O5	88.17 (9)	86.1224
C9-O5-Ni1	123.3(2)	122.2878	O2-Ni1-O2i	180	178.326	O1-Ni1-O5	91.83(9)	91.2787

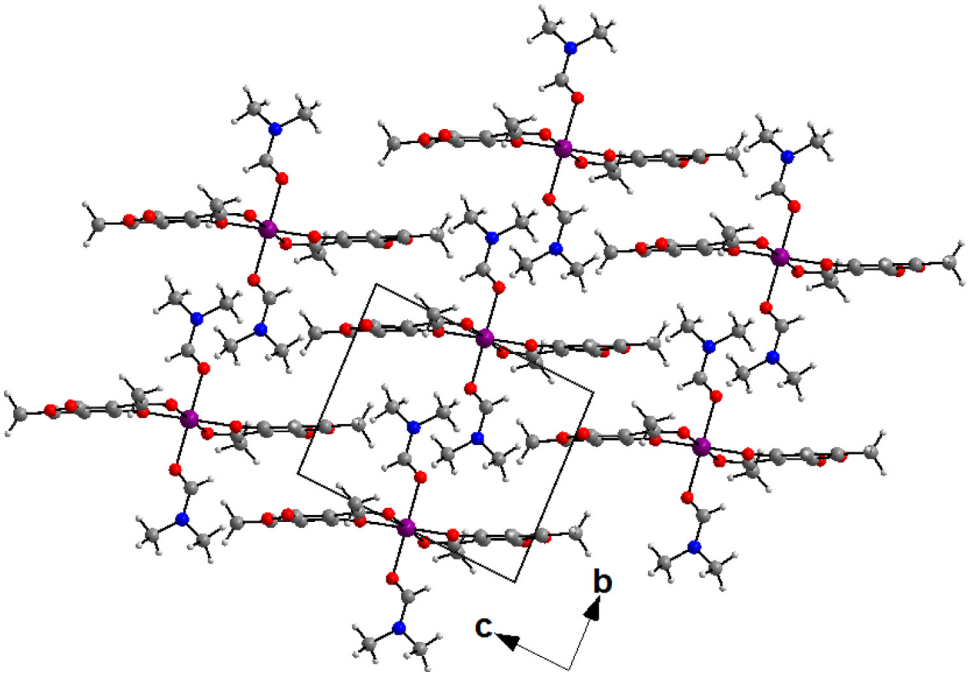

Fig. 2. Diagram packing of $[Ni(DHA)_2(DMF)_2]$ complex, showing an alternating parallel layers to (011) plane.

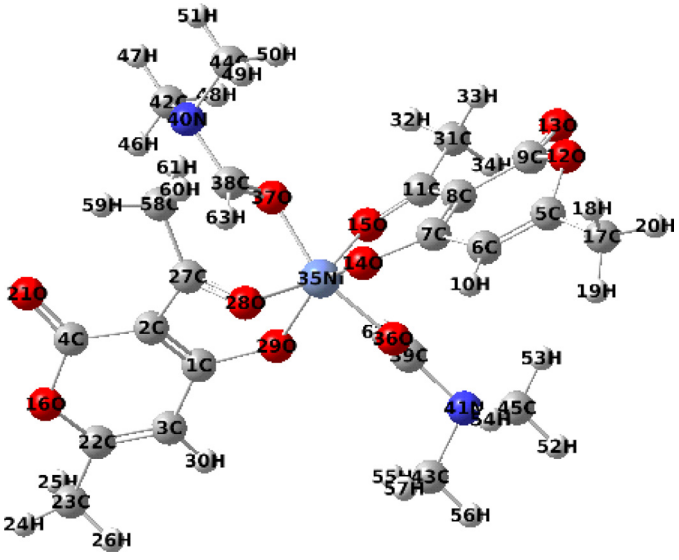

Fig. 3. Optimized structures of $[Ni(DHA)_2(DMF)_2]$ complex with the numbering of atoms computed from the B3LYP/6-31G (d,p) method.

is assigned to the C–N stretching vibration, which is in good agreement with the calculated wave number at 1334 cm^{-1}. The formation of the M–O bond is supported by the appearance of the ν(M–O) band in the region going from 420 to 620 cm^{-1} [42] which were computed in the range 420–654 cm^{-1}. This indicates that phenolic and ketonic oxygens atoms are involved in coordination. Additionally, the infrared spectrum of this complex displays strong bands for the aromatic C=C stretching bonds in the region 1350–1550 cm^{-1} which were in agreement with the calculated wave number at 1482 cm^{-1} and as well weak bands located in the region 2800–3200 cm^{-1} that can be attributed to the aromatic (Ph-H) and aliphatic (C–H) stretching vibration frequencies [43] while those calculated were detected in the region 2944–3275 cm^{-1}. As presented in Table 3 and Fig. 4, it can be noted that the experimental values have a better correlation when compared with those calculated. This confirms the validities of the optimized structures of $[Ni(DHA)_2(DMF)_2]$ complex.

3.2.3. Electronic absorption spectra

TD-DFT calculations of $[Ni(DHA)_2(DMF)_2]$ complex in gas phase were performed by using B3LYP-6-31G (d,p). The electronic absorp-

Table 3
The main experimental and calculated vibrational frequencies, their assignment, electronic absorption wavelengths, oscillator strengths (f_{os}) and excitation energy transitions of [Ni(DHA)$_2$(DMF)$_2$] complex, calculated by B3LYP/6-31G (d,p) method.

Vibrational frequencies (Exp./Calc.)					
υ $_{Exp.}$ (cm^{-1})	υ $_{Calc.}$ (cm^{-1})	Assignment	υ $_{Exp.}$ (cm^{-1})	υ $_{Calc.}$ (cm^{-1})	Assignment
3150	3275	υ $_{asym}$ (CH aromatic)	1352	1334	(C-N)
3200	3267	υ $_{sym}$ (CH aromatic)	1283	1265	(C-C)
2887	2944	υ $_{sym}$ (CH_3)	1051	1049	In-plane CH deformation mode w (CH_2)
1710	1702	υ (O-C=O)	779	792	Out-of-plane CH deformation mode
1690	1734	υ (C=O)	620	654	δ (Ni-O)
1489	1482	υ $_{asym}$ (C=C) aromatic	420	420	δ (Ni-O)
1443	1457	δ_{sym} (CH_3)	1352	1334	(C-N)

Electronic absorption wavelengths (Exp./Calc.)			
Exp.	TD-B3LYP		
DMSO	Gaz		
λ (nm)	λ (nm)	Osc. Strength ($f$os)	Excitation energy (eV/nm)
350	366	0.0004	0.6705
420	504	0.0021	0.5624

υ: stretching; υ_{sym}: symmetric stretching; υ_{asy}: asymmetric stretching; δ: deformation; ω: wagging.

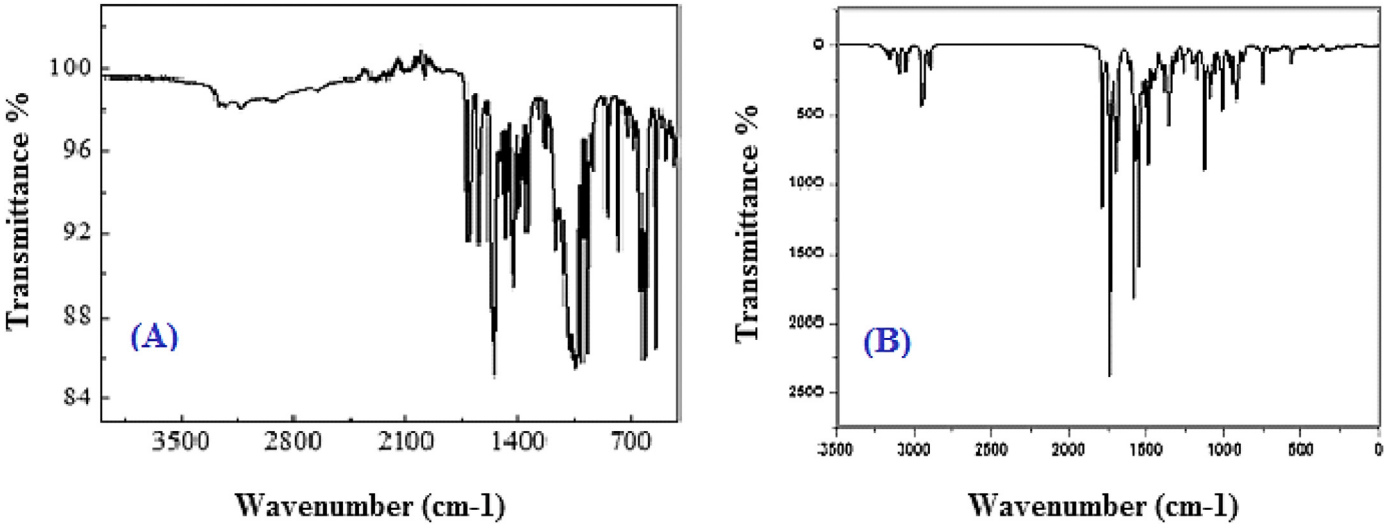

Fig. 4. FT-IR spectra of [Ni(DHA)$_2$(DMF)$_2$] complex: (A) Calculated spectrum by B3LYP/6-31G (d,p) and (B) Experimental spectrum in KBr.

tion wavelengths, oscillator strengths (f_{os}) and excitation energy transitions of this complex have been given in Table 3. Experimental and calculated spectra of the complex are given in Fig. 5. As compared with those calculated by TD-B3LYP level in gas phase. The absorption band for [Ni(DHA)$_2$(DMF)$_2$] complex appeared at 350 nm. The energy absorption band at 350 nm is 0.6705 eV with oscillator strength of 0.0021 at 366 nm, so this absorption can be assigned to n-π^* corresponding to the transitions of C=O chromophore [44]. This complex, showed also a weak broad band at 420 nm. The energy absorption band at 420 nm is 0.5624 eV with oscillator strength of 0.0004 at 504 nm. This absorption can be corresponding to the ligand-metal charge transfer transition (LMCT) [45]. It was observed that the results for hybrid potential B3LYP are slightly augmented and the finest values were found for B3LYP functional.

3.2.4. Frontier molecular orbitals studies

The highest occupied molecular orbital (HOMO) and the lowest unoccupied molecular orbital (LUMO) are frequently studied in order to impart key information regarding the electron-donor and electron-acceptor character of the complexes which shall lead to the interpretation of the charge transfer process [46]. The lower energy of the HOMO indicates the lower ability as an electron-

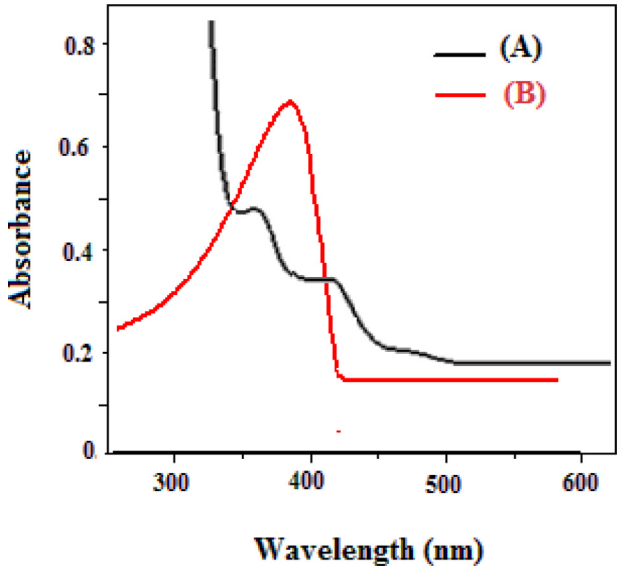

Fig. 5. Experimental (A) and calculated (B) electronic spectra of [Ni(DHA)$_2$(DMF)$_2$] complex.

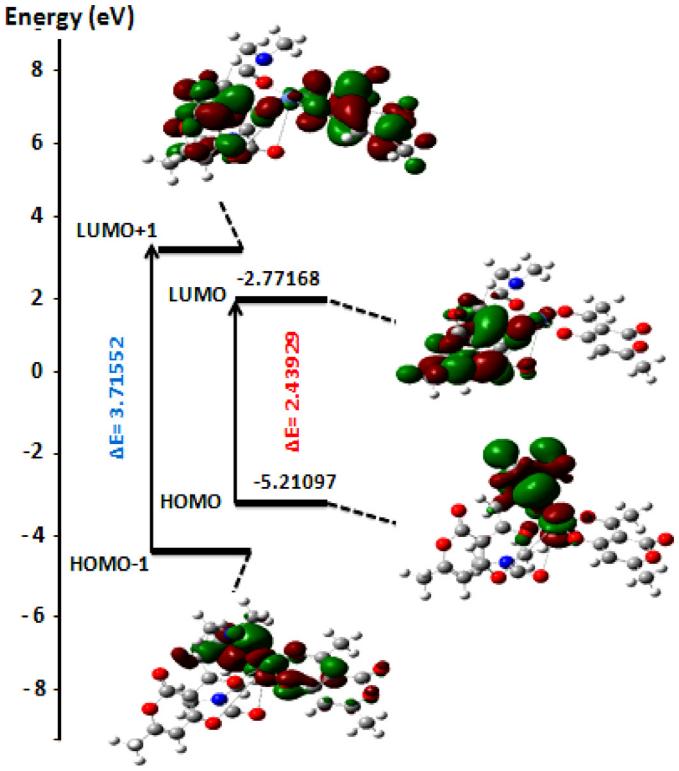

Fig. 6. HOMO-LUMO surfaces and energy gap for orbital's $[Ni(DHA)_2(DMF)_2]$ complex obtained with DFT-B3LYP/6-31G (d,p) method.

donor, resulting from the higher energy of LUMO and higher resistance to accept an electron. This allows elucidation of chemical stability by observing the difference in energy between HOMO and LUMO (Egap) while the large E_{gap} is preferred for the high stability of complex. The distribution of electron density of the $[Ni(DHA)_2(DMF)_2]$ complex is illustrated in the following Fig. 6. In addition, this study can also explain the chemical concept of chemical softness and hardness. With small E_{gap} values, the complex may be considered as a "soft" base due to its high energy of HOMO and therefore enhance the interaction with the LUMO of soft acids. Other than that, indices such as electron affinity and ionization potential are also commonly interconnected with the studies of HOMO and LUMO energies in pursuing a better grasp of how complex theoretically behave, chemical wise. The exchange–correlation functional: B3LYP was checked by comparing the results of the reactivity descriptors parameters data for $[Ni(DHA)_2(DMF)_2]$ complex as presented in Table 4. The given low energy gap (2.43929 eV) thus indicates high reactivity of the complex due to ease of charge transfer process [47]. The high value of softness (1.85776) or the low value of hardness (1.21964) indicates lower energy is needed for electron transition from HOMO to LUMO which means that the complex is susceptible to deform and ready to interact with other nucleophilic active site such as amino acid.

3.2.5. Mulliken atomic charges

The Mulliken atomic charges of $[Ni(DHA)_2(DMF)_2]$ complex were calculated by DFT using B3LYP 6-31G (d,p) at a basis set, the data were tabulated in Table S2. The Mulliken's atomic charges (Fig. 7) of the DFT calculation revealed a charge distribution in individual atoms. The charges on carbon atoms exhibited either positive or negative values. All hydrogen atoms displayed a neat positive charge and act as acceptor atoms. All oxygen atoms of the optimized compounds were shown to have a negative charge, which acts as donor atoms. The positively charged centers are the most susceptible sites for nucleophilic attacks i.e., electron donation. However, the most negatively charged centers are the most susceptible sites for electrophilic one [48].

3.2.6. Molecular electrostatic potential (MEP)

The molecular electrostatic potential (MEP) provides a visual method to understand the relative polarity of a molecule, electrostatic potential (electron + nuclei) distribution [49] and to find the reactive sites of molecules [50]. The molecular electrostatic potential of the studied complex is calculated using the B3LYP/6-31G (d,p) level and seen in Fig. 8. The total electron density mapped with electrostatic potential surface of the ligands are shown in Fig. 8A, The MEP mapped surface and electrostatic potential contour map for positive and negative potentials are also shown in Fig. 8B and C. As represented in this figure, the maximum negative region is the preferred sites for electrophilic attack, indicated as red color. So, an attacking electrophile will be attracted by the negatively charged sites, and the opposite situation for the blue re-

Table 4
Reactivity descriptors (in eV) and the different parameters of $[Ni(DHA)_2(DMF)_2]$ complex, computed at B3LYP/6-31G (d, p) level of theory.

Parameters	$[Ni(DHA)_2(DMF)_2]$	Parameters	$[Ni(DHA)_2(DMF)_2]$
E_{HOMO}	-5.21097	αxz	-6.8928
E_{LUMO}	-2.77168	αyz	2.2552
E_{HOMO-1}	-5.37036	$<\alpha>$	-197.436
E_{LUMO+1}	-1.65484	$\Delta\ \alpha°$	82.2806
Energy gap, $\Delta E_{GAP} = E_{HUMO}-E_{LUMO}$	2.43929	ßxxx	80.8624
$\Delta E_{GAP} = E_{HOMO-1}-E_{LUMO+1}$	3.71552	ßxxy	273.5802
Ionisation potential, $I= -E_{HOMO}$	5.21097	ßxyy	-32.8649
Electron affinity, $A = -E_{LUMO}$	2.77168	ßyyy	121.5724
Hardness, $\eta = 1/2(E_{LUMO}-E_{HOMO})$	1.21964	ßxxz	-69.2952
Softenss, $S = 1/2\eta$	1.85776	ßxyz	13.5037
Chemical potential, $\mu = -(I+A)/2$	-3.99132	ßyyz	15.8974
Absolute electronegativity, $\chi = (I+A)/2$	3.99132	ßxzz	7.8673
Electrophilicity, $\omega = \chi 2/2\eta$	6.53083	ßyzz	1.3970
μ_x	1.4800	ßzzz	1.7426
μ_y	5.4889		
μ_z	1.4007		
μ_{tot}	5.8550		
α_{xx}	-226.8982	ßtot	403.7822
α_{yy}	-145.0528	αxy	-6.8928
α_{zz}	-220.3571	αxz	2.2552
αxy	13.5244	αxz	-197.436

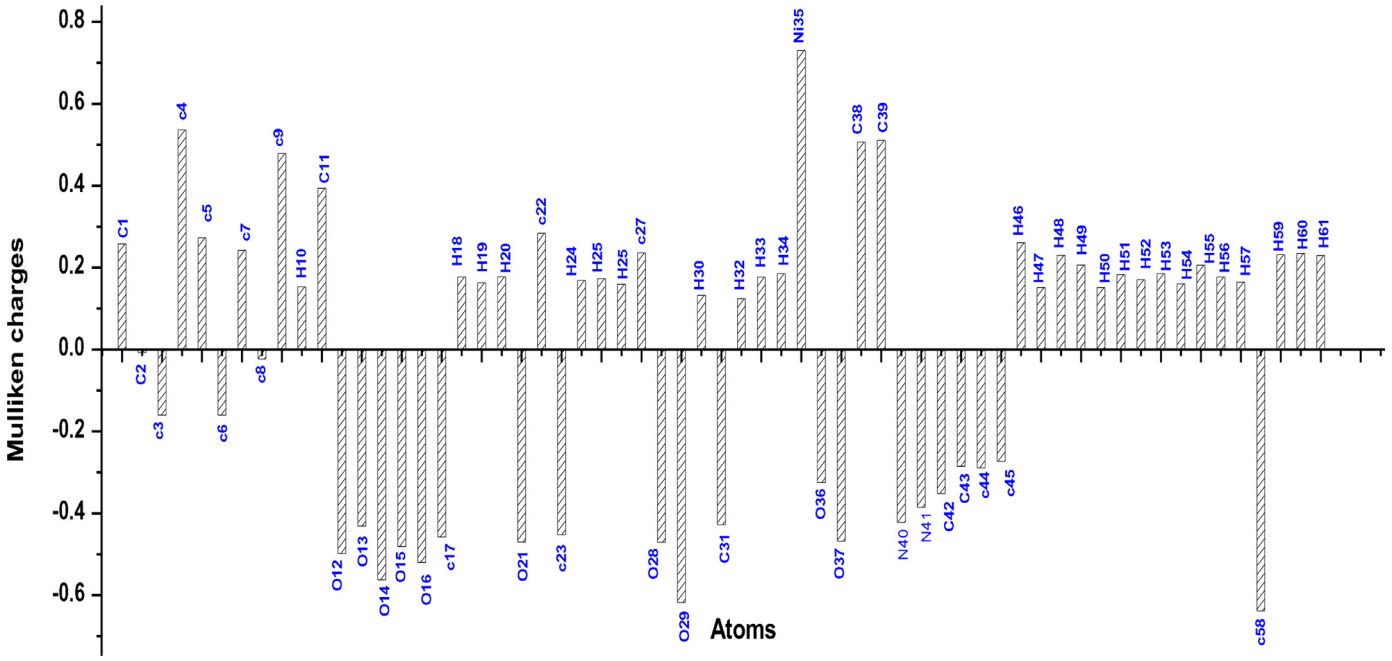

Fig. 7. The Mulliken atomic charge distribution of $[Ni(DHA)_2(DMF)_2]$ complex.

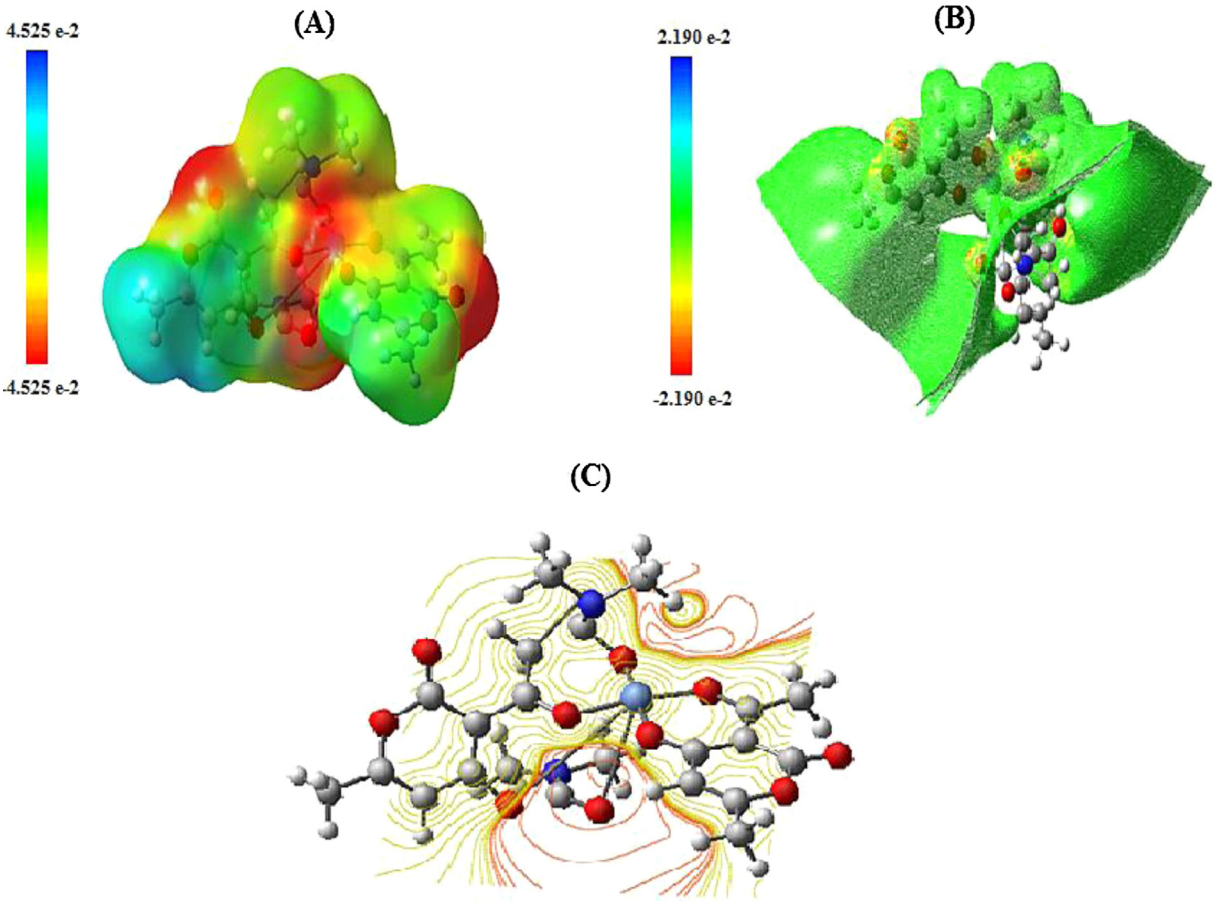

Fig. 8. (A) The total electron density surface mapped with electrostatic potential (MEP) plot of $[Ni(DHA)_2(DMF)_2]$ complex. Isovalue = 0.0004. Level of calculation: B3LYP/6-31G (d,p); (B) The electrostatic potential surface and (C) the contour map of electrostatic potential of $[Ni(DHA)_2(DMF)_2]$ complex.

gions. These negative and positive sites help to predict the regions where a compound is responsible of non-covalent interactions [51].

3.2.7. Nonlinear optical (NLO) properties

NLO properties such as molecular static polarizability (α), anisotropy of polarizability ($\Delta\alpha$) and first hyperpolarizability (ß) have been calculated by quantum chemical calculations with B3LYP/6-31G (d, p). The investigation of NLO character explores the non-centrosymmetric nature and architecture of the molecules. This can be achieved by positioning of appropriate donor-acceptor units and alteration of π-conjugation length [52–54]. The $<\alpha>$, $\Delta\alpha$ and $ß_{tot}$ parameters can be obtained by using following equations:

$$\langle\alpha\rangle = 1/3(\alpha_{xx} + \alpha_{yy} + \alpha_{zz}) \quad (1)$$

$$\Delta\alpha = 1/2\Big[(\alpha_{xx} - \alpha_{yy})^2 + (\alpha_{xx} - \alpha_{zz})^2 + (\alpha_{yy} - \alpha_{zz})^2 + 6\alpha^2{}_{xy} + 6\alpha^2{}_{xz} + 6\alpha^2{}_{yz}\Big]^{1/2} \quad (2)$$

$$\beta_{tot} = \Big[(ß_{xxx} + ß_{xyy} + ß_{xzz})^2 + (ß_{yyy} + ß_{yzz} + ß_{yxx})^2 + (ß_{zzz} + ß_{zxx} + ß_{zyy})^2\Big]^{1/2} \quad (3)$$

The molecular dipole moment, polarizability, anisotropy of polarizability and first hyperpolarizability of $[Ni(DHA)_2(DMF)_2]$ complex have been examined by using B3LYP/6-31G(d,p) level and tabulated in Table 4. The parameters μ_{tot}, $<\alpha>$, $\Delta\alpha$ and $ß_{tot}$ have been calculated as 5.8550 Debye, -197.436 a.u, 82.2806 a.u and 403.7822 a.u, respectively. Although the $[Ni(DHA)_2(DMF)_2]$ complex has aromatic ring and carbonyl (C=O) functional groups as well as high spin Ni(II) ion inducing the nonlinear optical parameters. As a consequence, the $[Ni(DHA)_2(DMF)_2]$ complex is a good candidate for NLO materials.

3.3. Electrochemical properties

The electrochemical behavior of $[Ni(DHA)_2(DMF)_2]$ complex was investigated by cyclic voltammetry (CV) using a GC electrode freshly polished immersed in electrolytic solution containing distilled H_2O + NaCl (10^{-1} M) and NaOH ($2{\cdot}10^{-1}$M) and 1 mM of nickel complex under nitrogen atmosphere, ambient temperature and potentials range going -1.5 to 1.8 V versus SCE at 100 mV s^{-1}.

Fig. S2 shows in the forward scan two oxidation waves at Epa1 = +770 mV/ SCE and Epa_2= +1256 mV/s. The first wave represents the oxidation of the nickel(II) species [55] according to the following Eq. (1):

$$Ni(II) \rightarrow Ni(III) + 1e- \quad (1)$$

While the second wave can be attributed to the oxidation of the ligand. On the back sweep, one cathodic reduction wave is only observed and appears at Epc1 = - 743 mV / SCE. This wave represents the reduction of the Ni(II) species into Ni(I) [56] as shown by the following electrochemical reaction:

$$Ni(II) + 1e- \rightarrow Ni(I) \quad (2)$$

When the electrode potential is scanned from 0.0 to +0.80 V, a reduction couple is discerned in the reverse scan, the half-wave potential located at $E_{1/2}$ = +753.5 mV/SCE and peak-to-peak separation estimated to about ΔE =180 mV can be assigned to the Ni(III)/Ni(II) redox couple [57]. The effect of the scan rate on the voltammetric response of the synthesized complex was also analyzed. Fig. S2 shows that the Ni(III)/Ni(II) redox couple seems to be dependent on the scan rates, especially for the anodic wave.

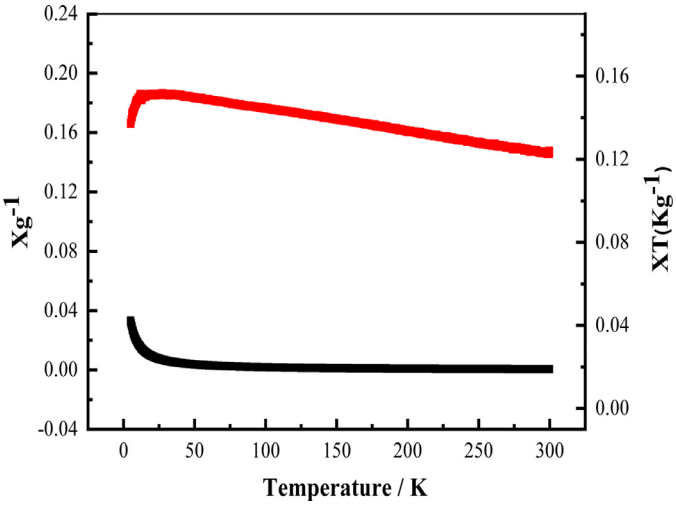

Fig. 9. The magnetic susceptibility variations χM (—) and χMT (—) as a function of temperature for $[Ni(DHA)_2(DMF)_2]$ complex.

Table 5
The magnetic data of the $[Ni(DHA)_2(DMF)_2]$ complex.

Temperature (K)	10^{-2} χM cm^3mol^{-1}	1 / χM mol cm^{-3}	μ_{eff} μb
10	6.8	14.7	1.88
20	6.44	15.52	2.95
30	5.37	18.62	2.26
50	3.5	27.93	3.05
75	1.77	56.49	2.1
100	1.43	69.93	2.73
150	1.074	93.1	2.89
200	0.716	139.66	2.73
250	0.358	279.32	2.15
300	0.332	301.2	2.24

This anodic wave, at low rates (5–100 mV s^{-1}), splits in two waves Epa(I) and Epa(II) becoming at higher scan rate 100 mV s^{-1} a unique wave. Here, it was observed that as the scan increases, both waves Epa(I) and Epc(II) shift to the more anodic and cathodic potentials, respectively. An increase in peak currents was as well noted [58]. However, it can also be observed that the current varies linearly with the root square of the scan rate indicating a diffusion redox process.

3.4. Magnetic properties

The magnetic behavior of $[Ni(DHA)_2(DMF)_2]$ is shown in Figs. 9–11. The temperature dependences of the susceptibility X are in the 5–300 K range, as X(T) and XT(T). The magnetic susceptibilities are positive and correspond to the paramagnetic state. The nickel complex shows a slight decrease in the magnetic susceptibility χT when the temperature drops from 12 K to 5 K. This, it corresponds in the occurrence of exchange interactions at the supramolecular level suggesting an antiferromagnetic coupling of nickel(II) ions, as described in the literature [59].

Molar susceptibility X_M = X. Molar weight/density
= 0.03 · 539.17/1.516
=X_M = 10.66 cm^3 mol^{-1}

The magnetic behavior of the sample was studied in the temperature range varied from 5 to 300 K (Table 5). The magnetic susceptibility of the Ni(II) complex changed with temperature according to the Curie–Weiss law. The magnetic properties of $[Ni(DHA)_2(DMF)_2]$ in the form of an χM vs. T plot (χM is the molar magnetic susceptibility) is shown in Figs. 10 and 11. The magnetic moment μ_{efft} of the compound is 3.05 BM at 50 K, indicating the presence of a high-spin of $[Ni(DHA)_2(DMF)_2]$ center, and

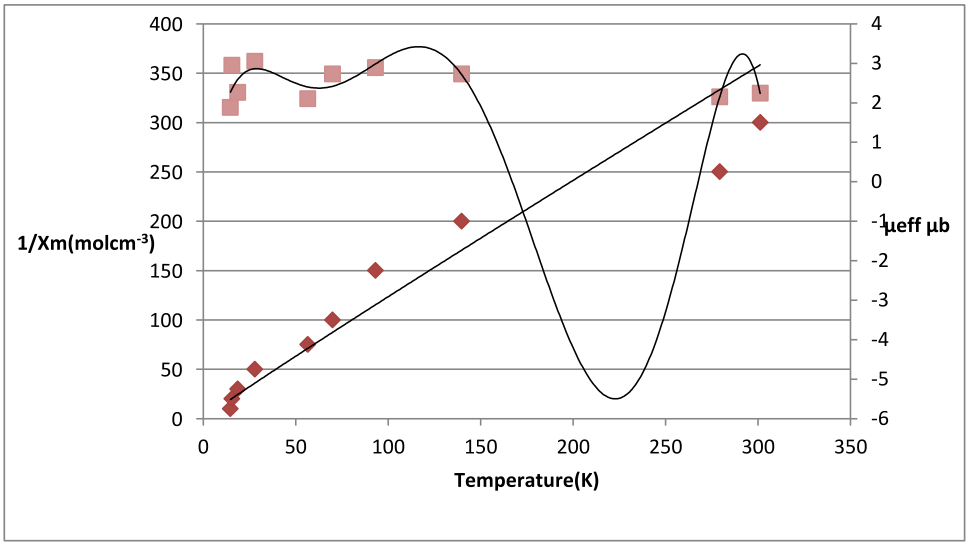

Fig. 10. Temperature dependence of 1/ χM and μ_{efft} for $[Ni(DHA)_2(DMF)_2]$ (1/ χM, μ_{efft}).

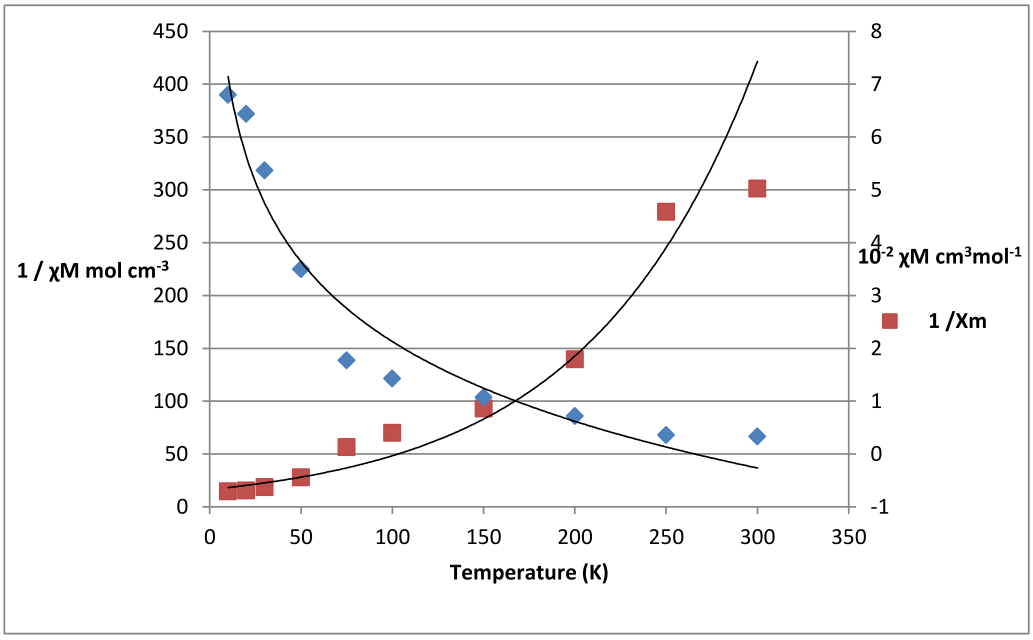

Fig. 11. Dependence between the magnetic susceptibility values vs. temperature.

seems to be in good conformity with those reported for high spin of hexa-coordinate Ni(II) complexes [60,61]. The temperature dependence of the magnetic susceptibility obeys to the Curie–Weiss law with a Weiss, indicating the absence of intermolecular interactions.

3.5. Molecular docking

3.5.1. Binding energy and molecular interaction of Docking studies

Molecular docking is a technique which explains how a molecule interacts with each other when it placed in a restricted system under a well-defined force field. It is widely used to predict and identify ligands that fit into the binding pocket of a protein of interest. The energy of interaction of the protein-drug complex, i.e., the binding energy is reflected in the docking score [62]. In this paper, the molecular docking is performed using the Molecular Operating Environment (MOE) 2019.0102 software to evaluate the binding mode of ligand and interactions in the active site. Our screening was performed against the key target of the main protease (M_{pro}) to identify a therapeutic agent of COVID-19.

Table 6 demonstrates the binding energies and different bonds of our complex. As compared to the inhibitor N3 (-7.44 kcal/mol), the $[Ni(DHA)_2(DMF)_2]$ complex exhibited a promising energy scores (-7.13) kcal/mol.

The active Mpro homodimer of SARS-CoV-2, according to the 3D structure, comprises two protomers, constituting three domains. Domain I contains 8–101 Amino acid residues, Domain II contains 102–184 Amino acid residues and amino acid residues 201–306 constitute Domain III. We have defined the Mpro binding site residues as Thr24, Thr25, Thr26, Leu27, His41, Met49, Tyr54, Phe140, Leu141, Asn142, Gly143, Ser144, Cys145, His163, His164, Met165, Glu166, Leu167, Pro168, His172, Asp187, Arg188, Gln189, Thr190, Ala191, and Gln192 residues.

Thr24, Thr26 and Asn119 are predicted to play important roles in drug interactions [63,64]. His163, His172 and Glu166 are believed to provide the opening gate for the substrate in the active

Table 6
Molecular docking results and interactions of the $[Ni(DHA)_2(DMF)_2]$ complex with SARS-CoV-2 Mpro.

Protein (Mpro)	Ligand	Binding energy Score (Kcal/mol)	RMSD refine	Bonds between atoms of compounds and residues of active site		
				Involved Receptor residues	Bond type	Bond length (Å)
	$[Ni(DHA)_2(DMF)_2]$ Complex	-7.1341	1.3245	Met 165 Cys 145 His 163	H-donor H-donor H-acceptor	3.45 3.803.53
	N3	-7.4401	1.1653	Cys 145 Cys 145 Glu 166 Gln 189 Gly 143 His 41 Asn 142	H-donor H-donor H-acceptor H-acceptor H-acceptor H-pi Pi-H	3.42 3.92 2.96 2.71 3.06 3.74 3.96

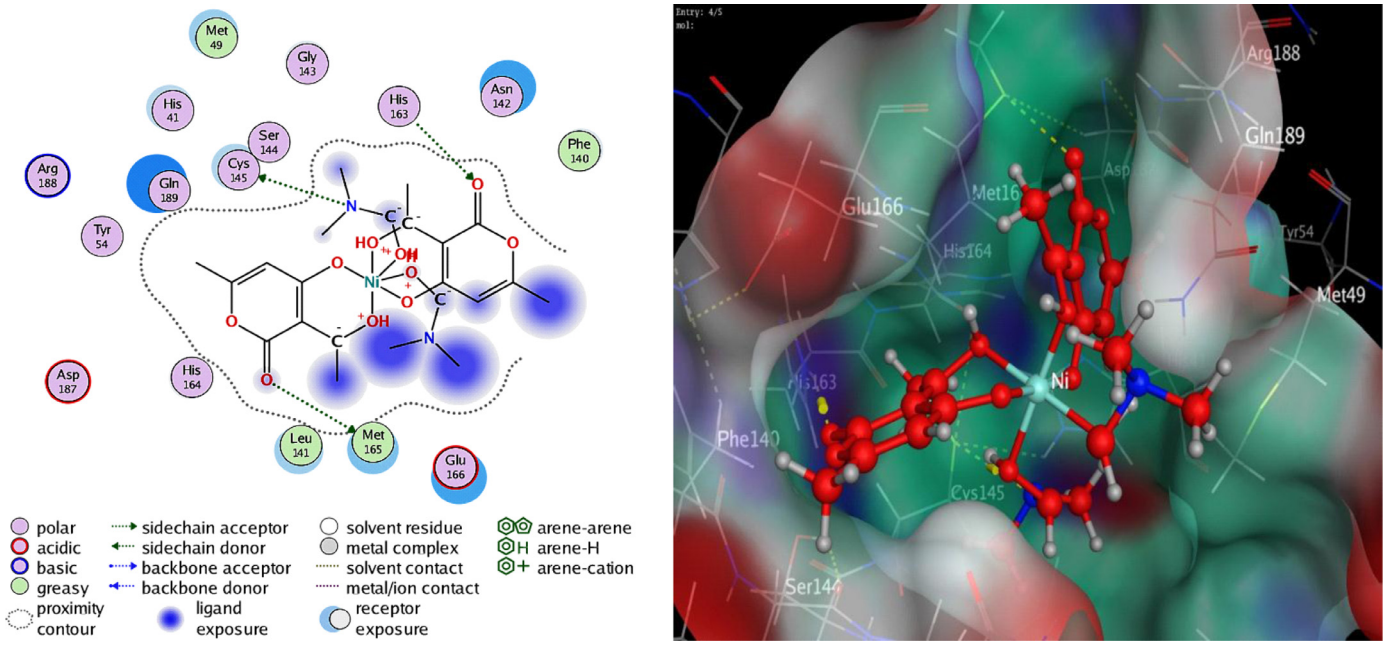

Fig. 12. 2D and 3D structure of the $[Ni(DHA)_2(DMF)_2]$ complex with SARS-CoV-2 Mpro.

state of the protomer [65], His41 and Cys145 form the catalytic dyad in the active site [66] and His164 is essential for the enzyme activity. Table 6 demonstrates the binding energies and different bonds of both standard ligand (N3) and complex. The docked N3 inside the COVID-19 virus Mpro pocket achieved a binding score of -7.44 kcal/mol beside the formation of two H-donor bonds with Cys 145, three H-acceptor bonds with Glu 166, Gln189 and Gly 143, one H-pi bond with His41 and one Pi-H with Asn 142. On the other hand, it was found that $[Ni(DHA)_2(DMF)_2]$ complex has a promising activity. Moreover, it has a very close binding energy scores (-7.13 kcal/mol) relative to the N3 inhibitor. The binding interactions of the docked $[Ni(DHA)_2(DMF)_2]$ complex demonstrated that it had three hydrogen bonds with Mpro, two donors at Met 165 and Cys 145 and one acceptor with His 163. These amino acids are predicted to play a major role during chemical interactions of Mpro inhibition. The detail of interaction and visualization of the docking results are provided in Fig. 12. It formed relatively stable complexes within the active site of M_{pro} with Hydrogen bonds, showed effective binding with CYS145 of catalytic dyad along with two interactions with other amino acid residues in active site of SARS CoV2-Mpro.

3.5.2. Screening through pharmacokinetic properties

During drug development, pharmacokinetics studies evaluate the concentration of drugs and their actions in the body. However, it demonstrates the movement of drug into the body after the administration of drug. The study Drug-like properties and pharmacokinetic properties is essential to assess the safety and efficacy of drugs and design appropriate regimens

Chemical descriptors calculation: Lipinski's rule of 5, Rules for the drug-likeliness, has been studied to ensure the drug-likeliness of $[Ni(DHA)_2(DMF)_2]$ complex drug ligands for SARS-CoV-2 Mpro protein and its number of violations. This Rule is able to predict absorption or permeation of a potential drug candidate combining specific parameters [4]. According to this, good oral bioavailability is more likely when there are Molecular weight (MW) not greater than 500 g/mol, a partition coefficient log P less than or equal five number of hydrogen bond donors (HBD) (NH and OH groups) not greater than five, and number of hydrogen bond acceptors (HBA) (O and N atoms) not exceeds ten (10). Drugs having log P ranging from 0 to 5, have high possibility of oral absorption. In general, an orally active drug has no more than one violation of these criteria. Violation of these parameters will reduce the draggability of the molecule [67].

As reported in Table 7, the tested complex followed Lipinski's rules for drug-likeness with no more than one violation. $[Ni(DHA)_2(DMF)_2]$ complex drug ligand exhibited two violation regarding hydrogen acceptor and molecular weight. Its molecular weight is slightly more than the recommended values but, within the permissible limit. $[Ni(DHA)_2(DMF)_2]$ complex showed the value of Log P less than five, which indicates that the molecules are more likely to be in the hydrophilic environment and are favorable for their drug-likeness.

The most popular and authentic rule for confirming the drug-likeness of the ligand is Lipinski's rule. However, many drugs have enormous pharmacological properties but, do not pass through the Lipinski's filter. They have been agreed by the FDA as possible drug for clinical purposes [68]. Despite violation of some rules, approved

Table 7
Detailed analyses of parameters of Lipinski's filter for the drug-likeness.

Ligand	MW	Lip acc	Lip-Don	Log p (o/w)	Lip drug- like	Violations
$[Ni(DHA)_2(DMF)_2]$	543.1950	12	04	3.5960	00	02

Table 8
ADME of the $[Ni(DHA)_2(DMF)_2]$ complex for SARS-CoV-2 Mpro.

Ligand	Solubility	Absorption			Distribution		Metabolism
	ADME Aqueous Solubility(Level)	Intestinal Absorption level	ADME AlogP98	ADME PSA-2D	BBB penetration level	Plasma Protein Binding	ADMECYP2D6 binding
$[Ni(DHA)_2(DMF)_2]$	-1.678 (4)	1	-1.052	112.747	4	False	False

anticancer and anti-infective drugs from natural products or their semi-synthetic derivatives such as taxol and amphotericin B have also some violations but, they are biologically effective as drugs. Therefore, these results do not interfere with the development of this complex SARS-CoV-2 therapeutic agent [69].

ADME parameters screening for drug likeness: The $[Ni(DHA)_2(DMF)_2]$ complex was screened using Discovery Studio 2.5 (Accelrys, San Diego, USA) software to predict their important pharmacokinetic properties. ADME properties include absorption, distribution, metabolism, excretion and hepatotoxicity (ADME) are considered as important in order to determine their role in drug discovery and success of the development of compound for human therapeutic use [70]. The screened results of ADME were summarized in Table 8, revealing eight descriptors, such as the absorption of drugs which depends on the intestinal absorption, polar surface area (PSA) and AlogP98.

ADME aqueous solubility predicts the solubility of the $[Ni(DHA)_2(DMF)_2]$ complex in water at 25°C. Descriptors of solubility predicts molar solubility of drugs within the ranges: < -8.0 (level 0 = extremely low solubility), -8.0 to -6.0 (level 1 = very low, but possible) -6.0 to -4.0 (level 2 = low), -4.0 to -2.0 (level 3 = good solubility), and -2.0 to 0.0 (level 4 = optimal solubility). ADME Aqueous solubility logarithmic level of the $[Ni(DHA)_2(DMF)_2]$ complex was found to be 4 which indicates optimal aqueous solubility. Human Intestinal Absorption (HIA) of drug after oral administration was determined by obtained levels: 0 (good), 1 (moderate), 2 (low), 3 (very low). $[Ni(DHA)_2(DMF)_2]$ complex was found to has moderate HIA, therefore it has an adequate gastro intestinal absorption. Easy distribution of the drug through blood brain barrier (BBB) measured by its AlogP98 value which must be less than 5. The obtained absorption levels determine drug absorption, it decreases inversely with the level, i.e., level 0 denotes proper absorption, level 1 denotes moderate absorption and so on. The intestinal absorption and blood brain barrier penetration were predicted by developing an ADME model using descriptors 2D PSA and AlogP98 that include 95% and 99% confidence ellipses. These ellipses define regions where well-absorbed compounds are expected to be found. Compounds with more than 90% absorbability would lie within the 99% confidence ellipse as the green ellipse Compounds falling out of the ellipse are those with less than 30% absorbability. As shown in Fig. 13, the results of DS-ADME model screening showed that $[Ni(DHA)_2(DMF)_2]$ complex within the 99% adsorption ellipse possess 99% confidence levels for human intestinal absorption. Table 8 shows that this complex has undefined values for BBB penetration level. Hence, the complex may not be able to penetrate the blood brain barrier. Hence, neurotoxicity of CNS with the proposed complex is not expected. ADME plasma protein binding model predicts whether a compound is likely to be highly bound to carrier proteins in the blood. True symbolizes binding and false symbolizes non-binding. The ADME plasma protein binding property prediction clearly suggests that the complex is not likely to be highly bound to carrier proteins in the blood. Metabolism is predicted based on the Cytochrome P450 2D6 inhibition. This descriptor determines inhibitory effect by the predicted classes: non-inhibitor (false) and inhibitor (true). $[Ni(DHA)_2(DMF)_2]$ complex is predicted as non-inhibitors of CYP2D6 suggesting that this complex is well metabolized in Phase-I metabolism. Hence, the side effects (i.e., liver dysfunction) are not expected upon administration of this complex.

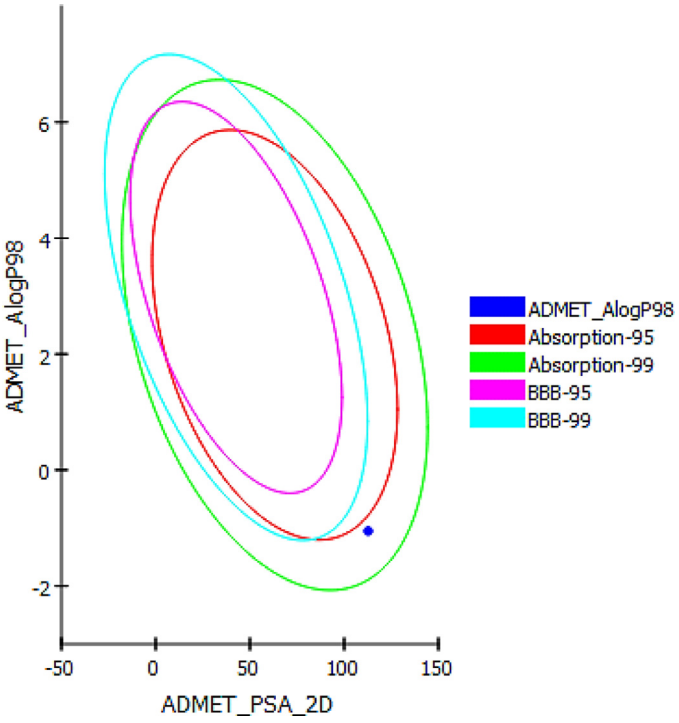

Fig. 13. Plot of polar surface area (PSA) versus ALogP for $[Ni(DHA)_2(DMF)_2]$ complex showing the 95% and 99% confidence limit ellipses corresponding to the blood brain barrier (BBB) and intestinal absorption.

Toxicity risks assessment: The toxicity predictions of the compounds were also investigated with Discovery Studio using the TOPKAT protocol. TOPKAT is a computational tool for prediction of toxicity of compounds developed by Accelrys [71]. It employs robust and cross-validated Quantitative Structure Toxicity Relationship (QSTR) models to predict a probable value of toxicity. The toxicity profiles calculated for all the compounds are tabulated in Table 9. The results indicate that $[Ni(DHA)_2(DMF)_2]$ complex is non-Mutagen, non-carcinogen with Mouse female and male NTP. Therefore, the toxicity of the ligands was found to be suitable for the development into a medical drug. Thus, they experiment significant first-pass effect.

Table 9
Virtual toxicity studies of $[Ni(DHA)_2(DMF)_2]$ complex.

Ligand	Ames mutagenicity	TOPKAT Mouse female NTP probability	TOPKAT Mouse male NTP probability	TOPKAT Daphnia EC_{50}(mg/L)
$[Ni(DHA)_2(DMF)_2]$	Non-mutagen	Non-carcinogen	Non-carcinogen	

4. Conclusions

Since December 2019, the COVID-19 consequences have severely affected the social life of human and also impacted the global economy. The growth of safer and extensive available strategies to overcome the increasing number of cases is greatly predicted. In this paper, we note the following results:

- A novel single crystal nickel(II)-complex has been synthesized and thoroughly characterized by conventional spectroscopic techniques, such as FT-IR, UV-Vis and cyclic voltammetry.
- The structural characterization supported by XRD-diffraction analysis of a single crystal has been used to define the molecular structure of the synthesized nickel complex.
- The electrochemical behavior of the nickel complex has also been investigated. The linear relationship observed between the anodic peak current (ip_a) and the square root of the scan rate ($v^{1/2}$) indicates that the electrochemical process is governed by diffusion.
- The geometry was optimized using DFT approach based on B3LYP/6-31G(d) allowing to explain the frontier molecular orbitals in gas phase. Meanwhile, TD-DFT methods were explored to better understanding the electronic transitions in the UV–Vis. spectrum.
- Obtained dipole moment, polarizability and hyperpolarizability values indicate that this nickel complex can be considered as an effective NLO materials.
- Finally, the molecular surfaces showed the electrophilic and nucleophilic regions on the nickel complex. Subsequently, this complex has been screened for its inhibitory effect against the main protease targets of SARS-CoV-2. A remarkable binding energy value, non-carcinogic and non-mutagenic properties have been shown.
- This study suggests that the screened complex could be further explored for structural modification and detailed investigations in order to synthesize as newer potent agents endowed with better anti SARS-CoV-2 therapeutic inhibition.
- As last conclusion, the diversification of this kind of studies will be considered as an efficient tool to master this disease.

Declaration of Competing Interest

The authors declare that they have no known competing financial interests or personal relationships that could have appeared to influence the work reported in this paper.

CRediT authorship contribution statement

Wassila Derafa: Writing – original draft, Formal analysis, Data curation. **Djouhra Aggoun:** Writing – review & editing, Writing – original draft, Conceptualization, Methodology, Supervision, Validation. **Zakia Messasma:** Methodology, Writing – review & editing. **Selma Houchi:** Formal analysis, Writing – review & editing. **Sofiane Bouacida:** Formal analysis. **Ali Ourari:** Validation, Writing – review & editing.

Acknowledgments

The authors thank the Algerian Ministry of Higher Education and Scientific Research (MESRS) and the Director General for Scientific Research and Technological Development (DGRSDT) for the financial support.

Supplementary materials

Supplementary material associated with this article can be found, in the online version, at doi:10.1016/j.molstruc.2022.133190.

References

[1] WHO coronavirus disease (COVID-19) dashboard, World Health Organization (2021) https://covid19.who.int/publicemergency.
[2] M.M. Lai, D. Cavanagh, The molecular biology of coronaviruses, Adv. Virus Res. 48 (1997) 1–100, doi:10.1016/S0065-3527(08)60286-9.
[3] Z. Jin, X. Du, Y. Xu, Y. Deng, M. Liu, Y. Zhao, B. Zhang, X. Li, L. Zhang, C. Peng, Y. Duan, J. Yu, L. Wang, K. Yang, F. Liu, R. Jiang, X. Yang, T. You, X. Liu, X. Yang, F. Bai, H. Liu, X. Liu, L.W. Guddat, W. Xu, G. Xiao, C. Qin, Z. Shi, H. Jiang, Z. Rao, H. Yang, Structure of M pro from SARS-CoV-2 and discovery of its inhibitors, Nature 582 (2020) 289–293, doi:10.1038/s41586-020-2223-y.
[4] T. Pillaiyar, M. Manickam, V. Namasivayam, Y. Hayashi, S.H. Jung, An overview of severe acute respiratory syndrome-coronavirus (SARS-CoV) 3CL protease inhibitors: peptidomimetics and small molecule chemotherapy, J. Med. Chem. 59 (2016) 6595–6628, doi:10.1021/acs.jmedchem.5b01461.
[5] L. Zhang, D. Lin, X. Sun, U. Curth, C. Drosten, L. Sauerhering, S. Becker, K. Rox, R. Hilgenfeld, Crystal structure of SARS-CoV-2 main protease provides a basis for design of improved α-ketoamide inhibitors, Science 368 (2020) 409–412, doi:10.1126/science.abb3405.
[6] F. Arndt, B. Eistert, H. Scholz, E. Aron, Zur synthese der dehydracetsäure aus acetessigester (Synthesis of dehydracetic acid from acetoacetic ester), Ber. Dtsch. Chem. Ges. 69 (1936) 2373–2380, doi:10.1002/cber.19360691030.
[7] A.M. Sarhan, S.A. Elsayed, M.M. Mashaly, A.M. El-Hendawy, Oxovanadium(IV) and ruthenium(II) carbonyl complexes of ONS-donor ligands derived from dehydroacetic acid and dithiocarbazate: Synthesis, characterization, antioxidant activity, DNA binding and *in vitro* cytotoxicity, Appl. Organomet. Chem. 33 (2018) e4655, doi:10.1002/aoc.4655.
[8] K. Lal, P. Yadav, A. Kumar, A. Kumar, A.K. Paul, Design, synthesis, characterization, antimicrobial evaluation and molecular modeling studies of some dehydroacetic acid-chalcone-1,2,3-triazole hybrids, Bioorg. Chem. 77 (2018) 236–244, doi:10.1016/j.bioorg.2018.01.016.
[9] A.G. Baldwin, J. Bevan, D. Brough, R. Ledder, S. Freeman, Synthesis and antibacterial activities of enamine derivatives of dehydroacetic acid, Med. Chem. Res. 27 (2018) 884–889, doi:10.1007/s00044-017-2110-8.
[10] S.P. Staforth, Bicyclic 6-6 systems: two heteroatoms 1:1, Comprehensive Heterocyclic Chemistry II (CHEC-II) 7 (1996) 527–559 https://doi.org/10.1016/B978-008096518-5.00159-3, doi:10.1016/B978-008096518-5.00159-3.
[11] S. Tekale, S. Mashele, O. Pooe, S. Thore, P. Kendrekar, R. Pawar, Biological Role of Chalcones in Medicinal Chemistry. Vect. Borne Dis. Recent Dev. Epidemiol. Control, (2020) 1–18. https://doi.org/10.5772/intechopen.91626.
[12] K.V. Tambov, I.V. Voevodina, A.V. Manaev, Y.A. Ivanenkov, N. Neamati, V.F. Traven, Structures and biological activity of cinnamoyl derivatives of coumarins and dehydroacetic acid and their boron difluoride complexes, Russ. Chem. Bull. 61 (2012) 78–90, doi:10.1007/s11172-012-0012-y.
[13] E. Mikami, T. Goto, T. Ohno, H. Matsumoto, M. Nishida, Simultaneous analysis of dehydroacetic acid, benzoic acid, sorbic acid and salicylic acid in cosmetic products by solid-phase extraction and high-performance liquid chromatography, J. Pharm. Biomed. Anal. 28 (2002) 261–267, doi:10.1016/S0731-7085(01)00564-7.
[14] Y. Li, H.E. Schellhorn, New developments and novel therapeutic perspectives for vitamin C, J. Nutr. 137 (2007) 2171–2184, doi:10.1093/jn/137.10.2171.
[15] (A) F. Zouchoune, S.-M. Zendaoui, N. Bouchakri, A. Djedouani, B. Zouchoune, Electronic structure and vibrational frequencies in dehydroacetic acid (DHA) transition-metal complexes: A DFT study, J. Mol. Struct. 945 (2010) 78–84, doi:10.1016/j.theochem.2010.01.015; (B) M.Z. Chalaça, J.D. Figueroa-Villar, J.A. Ellena, E.E. Castellano, Synthesis and structure of cadmium and zinc complexes of dehydroacetic acid,, Inorg. Chim. Acta 328 (2002) 45–52, doi:10.1016/S0020-1693(01)00672-7.
[16] (A) A. Kubaisi, K. Ismail, Nickel(I1) and palladium(II) chelates of dehydroacetic acid Schiff bases derived from thiosemicarbazide and hydrazinecarbodithioate, Can. J. Chem. 72 (1994) 1785–1788, doi:10.1139/v94-226; (B) A. Marir, T.N. Mouas, B. Anak, E. Jeanneau, A. Djedouani, L. Aribi-Zouioueche, F. Rabilloud, Cobalt(II), Nickel(II) and Zinc(II) complexes based on DHA: synthesis, X-ray crystal structure, antibacterial activity and DFT computational studies, J. Mol. Struct. 1217 (2020) 128353, doi:10.1016/j.molstruc.2020.128353.

[17] S.F. Tan, K.P. Ang, Unsymmetrical bis-Schiff bases derived from ethylenediamine, dehydroacetic acid and another aldehyde/ketone and the preparation and characterisation of their copper(II) and nickel(II) complexes, Trans. Met. Chem. 13 (1988) 64–68, doi:10.1007/BF01041502.

[18] S. Thabti, A. Djedouani, S. Rahmouni, R. Touzani, A. Bendaas, H. Mousser, A. Mousser, Synthesis, X-ray crystal structures and catecholase activity investigation of new chalcone ligands, J. Mol. Struct. 1102 (2015) 295–301, doi:10.1016/j.molstruc.2015.08.071.

[19] S. Tabti, A. Djedouani, D. Aggoun, I. Warad, S. Rahmouni, S. Romdhane, H. Fouzi, New Cu(II), Co(II) and Ni(II) complexes of chalcone derivatives: synthesis, X-ray crystal structure, electrochemical properties and DFT computational studies, J. Mol. Struct. 1155 (2018) 11–20, doi:10.1016/j.molstruc.2017.10.084.

[20] F.A. El-Saied, A.A. El-Asmy, W. Kaminsky, D.X. West, Spectral and structural studies of cobalt(II,III), nickel(II), and copper(II) complexes of dehydroacetic acid N4-dialkyl- and 3-azacyclothiosemicarbazones, Transit. Met. Chem. 28 (2003) 954–960, doi:10.1023/A:1026369419745.

[21] (A) A. Ourari, W. Derafa, S. Bouacida, D Aggoun, Catena-Poly[[[(pyridine-κN)copper(II)]-μ-3-{1-[(2-amino-eth-yl) imino]-eth-yl}-6-methyl-2-oxo-2H-pyran-4-olato-μ 4N,N,O 4:O 2] perchlorate], Acta Cryst. E67 (2011) m1720–m1721, doi:10.1107/S1600536811046411; (B) A. Ourari, W. Derafa, D. Aggoun, A novel copper(ii) complex with an unsymmetrical tridentate-Schiff base: synthesis, crystal structure, electrochemical, morphological and electrocatalytic behaviors toward electroreduction of alkyl and aryl halides, RSC Adv. 5 (2015) 82894–82905, doi:10.1039/C5RA10819E.

[22] A. Ourari, W. Derafa, S. Bouacida, D. Aggoun, J.C. Daran, Bis[μ-(3-acetyl-2-hydroxy-6-methyl-4H-pyran-4-one-κ3O:O′,O′′)]diaquatetrakis(pyridine-κN)dicopper(II) diperchlorate, Acta Crystallogr. E68 (2012) m1356–m1357, doi:10.1107/S1600536812041608.

[23] M.C. Burla, R. Caliandro, M. Camalli, B. Carrozzini, G.L. Cascarano, L. De Caro, C. Giacovazzo, G. Polidori, R. Spagna, SIR2004: an improved tool for crystal structure determination and refinement, J. Appl. Crystallogr. 38 (2005) 381–388, doi:10.1107/S002188980403225X.

[24] G.M. Sheldrick, A short history of SHELX, Acta Crystallogr. A 64 (2008) 112–122, doi:10.1107/S0108767307043930.

[25] L.J. Farrugia, WinGX and ORTEP for windows: an update, J. Appl. Crystalogr. 45 (2012) 849–854, doi:10.1107/S0021889812029111.

[26] L.J. Farrugia, ORTEP-3 for windows: a version of ORTEP-III with a graphical user interface (GUI), J. Appl. Crystallogr. 30 (1997) 565, doi:10.1107/S0021889897003117.

[27] K. Brandenburg, M. Berndt, DIAMOND. Crystal Impact, Bonn, 2001.

[28] A.C. Lee, W. Yang, R.G. Parr, Development of the Colic-Salvetti correlation-energy formula into a functional of the electron density, Phys. Rev. B 37 (1988) 785–789, doi:10.1103/PhysRevB.37.785.

[29] P. Salvador, B. Paizs, M. Duran, S. Suhai, On the effect of the BSSE on intermolecular potential energy surfaces. Comparison of a priori and a posteriori BSSE correction schemes, J. Comput. Chem. 22 (2001) 765–786, doi:10.1002/jcc.1042.

[30] M.E. Casida, D.P. Chong, Time-dependent density-functional response theory for molecules, Recent Advances in Density Functional Methods, Recent Advances in Density Functional Methods, 1, World Scientific, Singapore, 1995, doi:10.1142/9789812830586_0005.

[31] R.V. Leeuwen, Key concepts in time-dependent density-functional theory, Int. J. Mod. Phys. B 15 (2001) 1969–2023, doi:10.1142/S021797920100499X.

[32] 17.1.2 Marvin Sketch, Chem Axon (2017) http://www.chemaxon.com.

[33] HyperChem (Molecular Modeling System) Hypercube, Inc., Gainesville, FL 32601, USA, 2007 1115 NW, 4th Street http://www.hyperchem.com/ .

[34] C.A. Lipinski, F. Lombardo, B.W. Dominy, P.J. Feeney, Experimental and computational approaches to estimate solubility and permeability in drug discovery and development settings, Adv. Drug Deliv. Rev. 23 (1997) 3–25, doi:10.1016/S0169-409X(00)00129-0.

[35] M. Kwiatkowski, E. Kwiatkowski, A. Olechnowicz, D.M. Ho, E. Deutsch, New nickel(II) and palladium(II) complexes with unsymmetrical quadridentate Schiff bases derived from 8-amino-4- methyl-5-azaoct-3-en-2-one. Crystal and molecular structure of [4,10-dimethyl-3-(nitroso-χN)-5,9-(diaza-χ2N)-trideca-3,10- diene-2,12-(dionato-χO)(2−)]nickel(II), J. Chem. Soc. Dalton Trans. (1990) 2497–2502, doi:10.1039/DT9900002497.

[36] A. Ourari, I. Bougossa, S. Bouacida, D. Aggoun, R. Ruiz-Rosas, E. Morallon, H. Merazig, Synthesis, characterization and X-ray crystal structure of novel nickel Schiff base complexes and investigation of their catalytic activity in the electrocatalytic reduction of alkyl and aryl halides, J. Iran. Chem. Soc. 14 (2017) 703–715 10.1007/s13738-016-1022-8.

[37] F.H. Allen, O. Kennard, D.G. Watson, L. Brammer, A.G. Orpen, R. Taylor, Tables of bond lengths determined by X-ray and neutron difraction. Part 1. Bond lengths in organic compounds, J. Chem. Soc. Perkin Trans. 2 (1987) S1–S19, doi:10.1039/P298700000S1.

[38] P. Bhowmik, M.G.B. Drew, S. Chattopadhyay, Synthesis and characterization of nickel(II) and copper(II) complexes with tetradentate Schiff base ligands, Inorg. Chim. Acta 366 (2011) 62–67, doi:10.1016/j.ica.2010.10.010.

[39] F.F. Jian, P.S. Zhao, Z.S. Bai, L. Zhang, Quantum chemical calculation studies on 4-phenyl1-(propan-2-ylidene) thiosemicarbazide, Struct. Chem. 16 (2005) 635–639, doi:10.1007/s11224-005-8254-z.

[40] V.N. Patange, B.R. Arbad, Synthesis, spectral, thermal and biological studies of transition metal complexes of 4-hydroxy-3-[3-(4-hydroxyphenyl)- acryloyl]- 6-methyl-2H-pyran-2-one, J. Serb. Chem. Soc. 76 (2011) 1237–1246, doi:10.2298/JSC100531108P.

[41] B.T. Thaker, R.S. Barvalia, Bidentate coordinating behavior of chalcone based ligands towards oxocations: VO(IV) and Mo(V), Spectrochim. Acta A 112 (2013) 101–109, doi:10.1016/j.saa.2013.03.002.

[42] S.M. El-Megharbel, A.S. Megahed, M.S. Refat, Preparation, physical and chemical studies on metal complexes of Schif bases as a nucleus key to prepare nanometer oxides have catalytic applications: nickel(II) complexes derived from 4-aminoantipyrine derivatives, J. Mol. Liq. 216 (2016) 608–614, doi:10.1016/j.molliq.2016.01.097.

[43] M.L. Sundararajan, T. Jeyakumar, J. Anandakumaran, B.Karpanai Selvan, Synthesis of metal complexes involving Schiff base ligand with methylenedioxy moiety: spectral, thermal, XRD and antimicrobial studies, Spectrochim. Acta A 131 (2014) 82–93, doi:10.1016/j.saa.2014.04.055.

[44] R.M. Issa, A.M. Khedr, H.F. Rizk, UV–vis, IR and 1H NMR spectroscopic studies of some Schiff bases derivatives of 4-aminoantipyrine, Spectrochim. Acta A 62 (2005) 621–629, doi:10.1016/j.saa.2005.01.026.

[45] F. Karipcin, B. Dede, S. Percin-Ozkorucuklu, E. Kabalcilar, Mn(II), Co(II) and Ni(II) complexes of 4-(2- thiazolylazo)resorcinol: syntheses, characterization, catalase-like activity, thermal and electrochemical behaviour, Dye. Pigment. 84 (2010) 14–18, doi:10.1016/j.dyepig.2009.06.010.

[46] I. Fleming, Frontier Orbitals and Organic Chemical Reactions, Wiley, London, 1976, doi:10.1002/prac.19783200525.

[47] S. Kumar, A. Radha, M. Kour, R. Kumar, A. Chouaih, S.K. Pandey, DFT studies of disubstituted diphenyldithiophosphates of nickel(II): structural and some spectral parameters, J. Mol. Struct. 1185 (2019) 212–218, doi:10.1016/j.molstruc.2019.02.105.

[48] T.A. Yousef, Structural, optical, morphology characterization and DFT studies of nano sized Cu(II) complexes containing Schiff base using green synthesis, J. Mol. Struct. 1215 (2020) 128180, doi:10.1016/j.molstruc.2020.128180.

[49] A.E. Reed, F. Weinhold, Natural localized molecular orbitals, J. Chem. Phys. 83 (1985) 1736–1740, doi:10.1063/1.449360.

[50] E. Scrocco, J. Tomasi, The electrostatic molecular potential as a tool for the interpretation of molecular properties, in: New Concepts II. Topics in Current Chemistry Fortschritte der Chemischen Forschung, Springer, Berlin, Heidelberg, 1973, p. 42, doi:10.1007/3-540-06399-4_6.

[51] S.Y. Ebrahimipour, M. Abaszadeh, J. Castro, M. Seifi, Synthesis, X-ray crystal structure, DFTcalculation and catalytic activity of two new oxidovanadium(V) complexes containing ONO tridentate Schiff bases, Polyhedron 79 (2014) 138–150, doi:10.1016/j.poly.2014.04.069.

[52] M.U. Khan, M. Khalid, M. Ibrahim, A.A.C. Braga, M. Safdar, A.A. Al-Saadi, M.R.S.A. Janjua, First theoretical framework of triphenylamine–dicyanovinylene-based nonlinear optical dyes: structural modification of π-linkers, J. Phys. Chem. C 122 (2018) 4009–4018, doi:10.1021/acs.jpcc.7b12293.

[53] M.R.S.A. Janjua, M.U. Khan, B. Bashir, M.A. Iqbal, Y. Song, S.A.R. Naqvi, Z.A. Khan, Effect of π-conjugation spacer (CC) on the first hyperpolarizabilities of polymeric chain containing polyoxometalate cluster as a side-chain pendant: a DFT study, Comput. Theor. Chem. 994 (2012) 34–40, doi:10.1016/j.comptc.2012.06.011.

[54] M.R.S.A. Janjua, M. Amin, M. Ali, B. Bashir, M.U. Khan, M.A. Iqbal, W. Guan, L. Yan, Z.M. Su, A DFT study on the two-dimensional second-order nonlinear optical (NLO) response of terpyridine-substituted hexamolybdates: physical insight on 2D inorganic– organic hybrid functional materials, Eur. J. Inorg. Chem. 2012 (2012) 705–711, doi:10.1002/ejic.201101092.

[55] N. Bréfuel, C. Lepetit, S. Shova, F. Dahan, J.P. Tuchagues, Complexation to Fe(II), Ni(II), and Zn(II) of multidentate ligands resulting from condensation of 2-pyridinecarboxaldehyde with alpha, omega-triamines: selective imidazolidine/hexahydropyrimidine ring opening revisited, Inorg. Chem. 44 (2005) 8916–8928, doi:10.1021/ic050791b.

[56] M. Pooyan, A. Ghaffari, M. Behzad, H. Amiri Rudbari, G. Bruno, Tetradentate N_2O_2 type Nickel(II) Schiff base complexes derived from meso-1,2-diphenyle-1,2-ethylenediamine: synthesis, characterization, crystal structures, electrochemistry, and catalytic studies, J. Coord. Chem. 66 (2013) 4255–4267, doi:10.1080/00958972.2013.867031.

[57] D. Aggoun, Z. Messasma, B. Bouzerafa, R. Berenguer, E. Morallon, Y. Ouennoughi, A. Ourari, Synthesis, characterization and DFT investigation of new metal complexes of Ni(II), Mn(II) and VO(IV) containing N,O-donor Schiff base ligand, J. Mol. Struct. 1231 (2021) 129923, doi:10.1016/j.molstruc.2021.129923.

[58] R.S. Nicholson, Theory and application of cyclic voltammetry for measurement of electrode reaction kinetics, Anal. Chem. 37 (1965) 1351–1355, doi:10.1021/ac60230a016.

[59] M.J. Prushan, D.M. Tomezsko, S. Lofland, M. Zeller, A.D. Hunter, A nickel(II) di-μ2-phenolato bridged dinuclear complex: weak antiferromagnetic interactions in nickel(II) dimers, Inorg. Chim. Acta 360 (2007) 2245–2254, doi:10.1016/j.ica.2006.11.008.

[60] R. Vicente, A. Escuer, J. Ribas, Magnetic relationship in new Ni^{II}-Cu^{II}-Ni^{II} trinuclear complexes according to nickel(II) geometry, Polyhedron 11 (1992) 857–862, doi:10.1016/S0277-5387(00)83332-X.

[61] F. Jursík, B. Hájek, Transition metal complexes of ligands containing azomethine group. V. Stereochemistry and reactivity of four-coordinate nickel(II) complexes derived from (S)-(+)-cysteine derivatives, Inorg. Chim. Acta 13 (1975) 169–173, doi:10.1016/S0020-1693(00)90193-2.

[62] W.L. Jorgensen, The many roles of computation in drug discovery, Science 303 (2004) 1813–1818 https://www.science.org/doi/10.1126/science.1096361.

[63] X. Liu, X.J. Wang, Potential inhibitors against 2019-nCoV coronavirus M protease from clinically approved medicines, J. Genet. Genome 47 (2020) 119–121, doi:10.1016/j.jgg.2020.02.001.
[64] S.A. Khan, K. Zia, S. Ashraf, R. Uddin, Z. Ul-Haq, Identification of chymotrypsin-like protease inhibitors of SARS-CoV-2 via integrated computational approach, J. Biomol. Struct. Dyn. 39 (2021) 2607–2616, doi:10.1080/07391102.2020.1751298.
[65] H. Yang, M. Yang, Y. Ding, Y. Liu, Z. Lou, Z. Zhou, L. Sun, L. Mo, S. Ye, H. Pang, G.F. Gao, K. Anand, M. Bartlam, R. Hilgenfeld, Z. Rao, The crystal structures of severe acute respiratory syndrome virus main protease and its complex with an inhibitor, Proc. Natl. Acad. Sci. U. S. A. 100 (2003) 13190–13195, doi:10.1073/pnas.1835675100.
[66] M.T. Ul Qamar, S.M. Alqahtani, M.A. Alamri, L.L. Chen, Structural basis of SARS-CoV-2 3CL(pro) and anti- COVID-19 drug discovery from medicinal plants, J. Pharm. Anal. 10 (2020) 313–319, doi:10.1016/j.jpha.2020.03.009.
[67] R.N. Prinsa, D.G. Normi, M.D. Tejas, In search of SARS CoV-2 replication inhibitors: Virtual screening, molecular dynamics simulations and ADMET analysis, J. Mol. Struct. 1246 (2021) 131190, doi:10.1016/j.molstruc.2021.131190.
[68] D.S. Wishart, Y.D. Feunang, A.C. Guo, E.J. Lo, A. Marcu, J.R. Grant, T. Sajed, D. Johnson, C. Li, Z. Sayeeda, N. Assempour, I. Iynkkaran, Y. Liu, A. Maciejewski, N. Gale, A. Wilson, L. Chin, R. Cummings, D. Le, A. Pon, C. Knox, M. Wilson, DrugBank 5.0: a major update to the DrugBank database for 2018, Nucleic Acids Res. 8 (2017 Nov), doi:10.1093/nar/gkx1037.
[69] M.E. Abouelela, H.K. Assaf, R.A. Abdelhamid, E.S. Elkhyat, A.M. Sayed, T. Oszako, L. Belbahri, A.E. El Zowalaty, M.S.A. Abdelkader, Identification of potential SARS-CoV-2 main protease and spike protein inhibitors from the genus aloe: an in silico study for drug development, Molecules 26 (2021) 1767, doi:10.3390/molecules26061767.
[70] G. Prateeksha, T.S. Rana, A.K. Asthana, B.N. Singh, S.K. Barik, Screening of cryptogamic secondary metabolites as putative inhibitors of SARS-CoV-2 main protease and ribosomal binding domain of spike glycoprotein by molecular docking and molecular dynamics approaches, J. Mol. Struct. 1240 (2021) 130506, doi:10.1016/j.molstruc.2021.130506.
[71] G. Patlewicz, J.M. Fitzpatrick, Current and future perspectives on the development, evaluation, and application of in silico approaches for predicting toxicity, Chem. Res. Toxicol. 29 (2016) 438–451, doi:10.1021/acs.chemrestox.5b00388.